Contents lists available at ScienceDirect

Applied Catalysis B: Environmental

Ultrasonic chemical synthesis of hybrid mpg-C$_3$N$_4$/BiPO$_4$ heterostructured photocatalysts with improved visible light photocatalytic activity

Guoqiang Tan [a,*], Liaona She [a,b,**], Ting Liu [a], Chi Xu [a], Huijun Ren [a], Ao Xia [a]

[a] School of Materials Science and Engineering, Shaanxi University of Science & Technology, Xi'an, Shaanxi, 710021, China
[b] School of Materials Science and Engineering, Shaanxi Normal University, Xi'an 710062, China

ABSTRACT

Highly efficient mpg-C$_3$N$_4$/BiPO$_4$ heterostructured photocatalysts were successfully synthesized via a facile ultrasonic chemical method. The structure, morphology, surface composition and chemical state of mpg-C$_3$N$_4$/BiPO$_4$ hybrid photocatalysts were characterized by XRD, TEM, FTIR and XPS, respectively. Their photocatalytic activity was evaluated under visible light, UV light and solar light irradiation against the photodegradation of rhodamine B (RhB). BiPO$_4$ nanorod was anchored on the surface of mpg-C$_3$N$_4$ nanosheets and the strong electrostatic interaction between mpg-C$_3$N$_4$ and BiPO$_4$ facilitated the formation of mpg-C$_3$N$_4$/BiPO$_4$ heterostructure. Under visible light irradiation, $^{\bullet}$O$_2{}^-$ and h$^+$ were the two primary active species. BiPO$_4$ served as an electron trap to efficiently promote the separation of photogenerated electron-hole pairs. The electrons in the CB of both BiPO$_4$ and mpg-C$_3$N$_4$ could react with O$_2$ adsorbed onto the surface of BiPO$_4$/mpg-C$_3$N$_4$ and reduce it to form $^{\bullet}$O$_2{}^-$, the holes left behind in the VB of mpg-C$_3$N$_4$ could not directly oxidize OH$^-$ or H$_2$O to form $^{\bullet}$OH. The 9.5CN/0.5BPO could degrade 92.3% of RhB in 30 min, which was about 1.3 times as high as that of mpg-C$_3$N$_4$. The TOC removal rate of 9.5CN/0.5BPO was 1.23 times higher than that of mpg-C$_3$N$_4$. Under UV light irradiation, $^{\bullet}$O^{2-}, h$^+$ and $^{\bullet}$OH were the primary active species, the inhibition degree followed the order BQ > EDTA-2Na > TBA. The electrons in the CB of both BiPO$_4$ and mpg-C$_3$N$_4$ could react with O$_2$ to generate $^{\bullet}$O$_2{}^-$, the holes in the VB of BiPO$_4$ could react with OH$^-$ or H$_2$O to produce $^{\bullet}$OH. The 9.5CN/0.5BPO could degrade 94.3% of RhB in 6 min, which was approximately 4.2 times higher than that of BiPO$_4$ and 1.5 times larger than that of mpg-C$_3$N$_4$. The TOC removal rate of 9.5CN/0.5BPO was 6.98 times higher than that of P25. HPLC analysis proved that the destruction of the conjugated structure of RhB would be the major process. Based on the experimental results, a possible charge transfer mechanism for the enhanced visible and UV light photocatalytic activity was proposed.

© 2017 Elsevier B.V. All rights reserved.

1. Introduction

In recent years, with increasing environment pollution and energy crisis, semiconductor-based heterogeneous photocatalysis, as a promising alternative technology for dye degradation, hydrogen evolution and CO$_2$ reduction, has attracted considerable attention for its application in solar energy conversion and environmental remediation [1–8]. The traditional photocatalyst TiO$_2$ is very effective in the photocatalytic degradation of organic pollutants and hydrogen production because of its high photocatalytic activity and good stability. Nevertheless, the application of TiO$_2$ is largely limited as a result of its intrinsic wide band gap (3.2 eV), which could only absorbed the ultraviolet light, and high recombination rate of photoinduced electrons and holes [9,10]. Accordingly, it is of great significance and necessity to exploit novel photocatalysts with visible-light response as well as high efficient photogenerated charge separation.

Recently, BiPO$_4$ has attracted increasing attention since Zhu's group found monoclinic BiPO$_4$ exhibited much higher photocatalytic activity than P25 (TiO$_2$) for degradation of organic pollutants under UV light irradiation [11]. Nevertheless, the relative wide band gap (3.85 eV) restricts its photocatalytic activity only to be active in the UV light region that occupies no more than 4% of the solar spectrum [12,13]. In this regard, many strategies have been employed

to overcome this limitation through constructing heterostructures with other narrow bandgap semiconductors [14–18]. Despite this, it is still necessary to search for suitable components to combine with $BiPO_4$ for extending the light response range, facilitating photogenerated electron-hole separation, and remarkably improving the visible light photocatalytic activity of $BiPO_4$ [15].

Recently, a polymeric metal-free photocatalyst, graphite-like carbon nitride ($g-C_3N_4$) with a medium band gap of 2.7 eV, was reported by Wang et al., exhibiting good photocatalytic activity for hydrogen and oxygen evolution from water under visible light irradiation [19]. $G-C_3N_4$ had attracted great interest for its applications in water splitting [20–23], environmental pollutants degradation [24,25], CO_2 reduction [26–29] and fuel cells [30] owing to its excellent stability, appealing electronic structure, low cost and facile synthesis [31]. Nevertheless, the photocatalytic activity of bulk $g-C_3N_4$ was poor under visible light irradiation due to its low specific surface area and poor quantum yield [32,33]. Therefore, numerous strategies have been adopted to modify bulk $g-C_3N_4$. In order to increase the surface area and offer more active sites for photocatalytic reaction, mesoporous $g-C_3N_4$ ($mpg-C_3N_4$) was synthesized using various silica templates [34–36]. Via introducing mesoporosity into the $g-C_3N_4$, the light harvesting ability and the reactant adsorption capability of $g-C_3N_4$ were enhanced owing to its high specific surface area and multiple scattering effects [37]. Hence, $mpg-C_3N_4$ exhibited superior photocatalytic activity than bulk $g-C_3N_4$. In addition, extensive efforts have been exploited to increase the quantum yield of $g-C_3N_4$, for example, metal or nonmetal doping [38,39], dye sensitization [40], coupling with noble metal [41] and building heterostructures [42–44]. Among these methods, constructing heterostructures through coupling $g-C_3N_4$ with other appropriate semiconductors is an effective measure to promote the separation of photogenerated electron-hole pairs, leading to an enhanced quantum yield. $BiPO_4$ was also used to combine with $g-C_3N_4$ to form heterostructured composites. For example, Pan et al. has successfully prepared core-shell structured $C_3N_4/BiPO_4$ photocatalyst via a facile ultrasonic dispersion method and found that its photocatalytic activity was greatly enhanced, which may be due to the high separation rate of photogenerated carriers at the heterojunction interface derived from the energy level match between C_3N_4 and $BiPO_4$ [5]. Zou et al. synthesized an inorganic-organic $BiPO_4/g-C_3N_4$ photocatalyst by wet impregnation with calcination method, which exhibited a higher photocatalytic activity for the degradation of gaseous toluene compared to pure $g-C_3N_4$ [45]. Li et al. reported that hexagonal phase $BiPO_4$/mesoporous $g-C_3N_4$ and $g-C_3N_4$ quantum dot/hexagonal phase $BiPO_4$ were fabricated and used to degrade MO dye in liquid phase [46,47]. However, seldom attention has been paid to the photocatalytic mechanism of $mpg-C_3N_4/BiPO_4$ (monoclinic phase) heterojunctions under visible and UV light irradiation, which has remained unclear to date.

In the present study, we reported a novel $mpg-C_3N_4/BiPO_4$ heterostructured photocatalyst by a facile ultrasonic chemical method. The $mpg-C_3N_4/BiPO_4$ composites exhibited enhanced photocatalytic activity beyond that of either $mpg-C_3N_4$ or $BiPO_4$, as demonstrated by the degradation of RhB under visible, UV and sun light irradiation. The strong electrostatic interaction between $mpg-C_3N_4$ and $BiPO_4$ contributed to the improved separation efficiency of photogenerated charge and hence resulted in enhanced photocatalytic activity. The active species involved in the degradation of RhB were unambiguously determined under visible and UV light irradiation, and the corresponding photocatalytic mechanism was proposed. Moreover, the as-prepared $mpg-C_3N_4/BiPO_4$ composites had no selectivity and could effectively degrade different kinds of organic pollutants (RhB, MO and phenol). This work may provide a useful insight for the synthesis of heterostructured photocatalyst with enhanced photocatalytic activity.

2. Experimental

2.1. Preparation

All chemicals were of reagent grade and used without any further purification. The $mpg-C_3N_4$ powders were synthesized according to the previously reported method [48]. First, 10.0 g of melamine was dissolved in 40 mL of silica colloidal solution, and the mixture was heated at 100 °C with stirring to allow water to evaporate. Second, the dried powder was put into an alumina crucible with a cover and calcined at 550 °C for 4 h in a muffle furnace at a heating rate of 20 °C min^{-1}. Finally, the resulting light-yellow powder was treated with 400 mL of 4 mol/L NH_4HF_2 solution for 48 h to remove the silica template. The last yellow powder was washed for several times with deionized water and ethanol and dried at 70 °C for 12 h. The bulk $g-C_3N_4$ was synthesized by directly heating 10 g of melamine in a ceramic combustion boat, which was heated in a muffle furnace at a heating rate of 20 °C min^{-1} up to 550 °C and held for 4 h (Fig. S1).

$BiPO_4$ was synthesized via a facile microwave hydrothermal process. In a typical procedure, 3 mmol of $Bi(NO_3)_3·5H_2O$ and an equal molar of $Na_3PO_4·12H_2O$ were put simultaneously into a beaker. Then, 45 mL of distilled water and 5 mL of dilute nitric acid (1 mol/L) were added into the beaker and magnetically stirred at room temperature for 30 min to form a homogeneous solution. Subsequently, the obtained mixture was moved to a 100-mL Teflon-lined stainless steel autoclave. The microwave hydrothermal reaction was carried out at 200 °C for 60 min. After cooling to room temperature, the as-prepared precipitate was collected and washed with distilled water and anhydrous ethanol for three times, and then dried at 80 °C overnight.

The typical preparation procedure of the $mpg-C_3N_4/BiPO_4$ composite photocatalysts was as follows: first, an appropriate amount of $mpg-C_3N_4$ was ultrasonically dispersed in 50 mL ethanol for 3 h. Then, the as-prepared $BiPO_4$ powder was subsequently added into the above solution and sonicated for another 2 h. Finally, the produced suspension was stirred in a fume hood for 24 h and then dried at 80 °C for 12 h. According to this method, different mass ratios of $mpg-C_3N_4$ and $BiPO_4$ from 4:6 to 9.9:0.1 were synthesized and denoted as 4CN/6BPO, 5CN/5BPO, 7CN/3BPO, 9CN/1BPO, 9.5CN/0.5BPO and 9.9CN/0.1BPO, respectively. As a reference, a mechanically mixed 9.5MCN/0.5BPO (the mass ratio of $mpg-C_3N_4$ and $BiPO_4$ was 9.5:0.5) was obtained by grinding $mpg-C_3N_4$ and $BiPO_4$ powders together. Moreover, in order to compare photocatalytic activity with 9.5CN/0.5BPO, 9.5GCN/0.5BPO (the mass ratio of $g-C_3N_4$ and $BiPO_4$ was 9.5:0.5) was also prepared (Fig. S1).

2.2. Characterization

The crystalline structure of the samples was investigated using X-ray diffraction (XRD; D/max-2200PC) with Cu Kα radiation (λ = 1.5406 Å) in the range of 10–70° (2θ). The morphology and microstructure of the samples were examined by transmission electron microscopy (TEM; G^{2}F20 S-TWIN). Infrared spectra were obtained using a Fourier transform infrared (FT-IR; VECTOR-22) spectrometer. The surface analysis was examined by X-ray photoelectron spectroscopy (XPS; XSAM800). The photoabsorption performance was characterized by a UV–vis diffuse reflectance spectroscopy (DRS; Agilent Cary 5000) in the range of 200–800 nm, with $BaSO_4$ for the corrected baseline. The total organic carbon (TOC) content of the samples was analyzed by a total organic carbon analyzer (TOC; Liqui TOC II). N_2 adsorption-desorption analysis was carried out on a Micromeritics ASAP2460 instrument. The concentration of Bi ions in the solution after the photocatalytic operation was determined by inductively coupled plasma optical emission spectrometry (ICP-OES; Agilent 5100) analysis. To

probe the active species generated in the photocatalytic system, 1 mM benzoquinone (BQ) (superoxide radical scavenger), 1 mM *tert*-butyl alcohol (TBA) (hydroxyl radical scavenger) and 1 mM disodium ethylenediaminetetraacetate (EDTA-2Na) (hole scavenger) were introduced into the solution of RhB prior to addition of the photocatalyst.

2.3. Photocatalytic experiments

The photocatalytic activities of the samples were evaluated by the degradation of three typical dyes (Rhodamine B (RhB), methyl orange (MO) and phenol) under visible, UV and solar light irradiation, the initial concentration of which were all 5 mg/L. A 300 W high-pressure mercury lamp was used as the UV light source, a 500 W xenon lamp with a UV-cutoff filter ($\lambda \geq 420$ nm) was used as the visible light source and a 500 W xenon lamp was used as the solar light source. In a typical photocatalytic experiment, 0.05 g of photocatalyst powder was suspended in 50 mL of dye (RhB, MO or phenol) solution. Prior to light irradiation, the solution was stirred in darkness for 30 min in order to reach the adsorption/desorption equilibrium. At a certain period of time, 5 mL of suspension was withdrawn regularly and centrifuged to remove the photocatalyst. Then the concentration of dye in the supernatant was analyzed using a UV–vis spectrophotometer (SP-756p). The photocatalytic degradation products of RhB were analyzed by high performance liquid chromatography (HPLC; waters e2695) equipped with a UV–vis detector using a C18 inversed-phase column (250×4.6 mm, 5 μm) at 550 nm. The mobile phase was a mixture of methanol and water (V:V = 6:4) with a flow rate of 0.8 mL min^{-1}.

2.4. Photoelectrochemical measurements

All the photoelectrochemical measurements were performed on an electrochemical workstation (CHI660E) in a standard three-electrode system with the as-prepared samples as the working electrode, a platinum wire as the counter electrode, and Ag/AgCl (saturated KCl) as the reference electrode. The working electrodes were prepared as follows: a total of 0.1 g photocatalyst was added into the mixed solution of 1 mL of anhydrous ethanol and 0.1 mL of acetyl acetone. After a period of time, it turned into a homogeneous suspension with ultrasonic dispersion. Then, the as-prepared suspension was spread on a 1.5×2 cm^2 fluorine-doped tin oxide (FTO) conducting glass with spin-coating method for 2 times. The film electrodes were dried under ambient condition and then calcinated at 150 °C for 3 h. A 500 W Xe arc lamp was used as the visible light source and a 300 W mercury lamp was utilized as the UV light source. A 0.1 M Na$_2$SO$_4$ aqueous solution was used as the electrolyte. The electrochemical impedance spectra (EIS) were interpreted by a nonlinear least-squares fitting procedure using the ZsimpWin software.

3. Results and discussion

3.1. Characterizations of mpg-C$_3$N$_4$/BiPO$_4$ composites

Fig. 1 displayed the typical XRD patterns of mpg-C$_3$N$_4$/BiPO$_4$ composites with different mass ratios, together with those of mpg-C$_3$N$_4$ and BiPO$_4$. For the mpg-C$_3$N$_4$, the diffraction peak located at 27.4° corresponded to the characteristic interplanar staking peak of the conjugated aromatic system, which was indexed to the (002) crystal plane, whereas the diffraction peak at 2θ value of 13.0° corresponded to a distance d = 0.679 nm and was indexed as the (100) diffraction plane of mpg-C$_3$N$_4$ (JCPDS NO. 87-1526) [49,50]. The diffraction peaks at 2θ of 18.4°, 21.3°, 30.3°, 37.2°, 43.2° and 57.1° were attributed to (111), (200), (220), (222), (400)
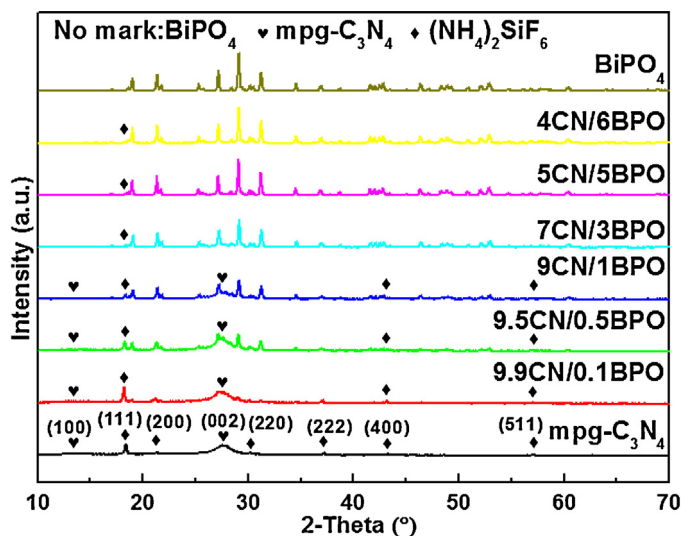

Fig. 1. XRD patterns of mpg-C$_3$N$_4$, BiPO$_4$ and mpg-C$_3$N$_4$/BiPO$_4$ composites with different mass ratios.

and (511) planes of (NH$_4$)$_2$SiF$_6$'s cubic structure (JCPDS NO. 72-1759), respectively, indicating that the mpg-C$_3$N$_4$ was not thoroughly washed with distilled water and absolute ethyl alcohol. For the BiPO$_4$, a series of sharp and well-defined diffraction peaks were observed, which was in accordance with the BiPO$_4$ phase with space group P21/n for monoclinic structure (JCPDS NO. 89-0287). With respect to the mpg-C$_3$N$_4$/BiPO$_4$ hybrids, no diffraction peaks of mpg-C$_3$N$_4$ appeared in the XRD patterns of the 4CN/6BPO, 5CN/5BPO and 7CN/3BPO samples, this may be attributed to the fact that the mpg-C$_3$N$_4$ layers were too thin. With increasing the mass ratio of mpg-C$_3$N$_4$ and BiPO$_4$ from 9:1 to 9.9:0.1, the typical diffraction peaks belonging to mpg-C$_3$N$_4$ gradually appeared. From 4CN/6BPO to 9.9CN/0.1BPO, the characteristic peak intensities of BiPO$_4$ were gradually decreased, which may be ascribed to the increased mpg-C$_3$N$_4$ content in the composites. The intensity of (111) diffraction peak assigned to (NH$_4$)$_2$SiF$_6$ was increased gradually with increasing the mass ratio of mpg-C$_3$N$_4$ and BiPO$_4$ from 4:6 to 9.9:0.1. Furthermore, the (400) and (511) diffraction peaks belonging to (NH$_4$)$_2$SiF$_6$ gradually appeared from 9CN/1BPO to 9.9CN/0.1BPO, while other diffraction peaks of (NH$_4$)$_2$SiF$_6$ were not easily observed in the XRD patterns, due to the close peak position of BiPO$_4$ and (NH$_4$)$_2$SiF$_6$ at 21.3°, 30.3° and 37.2°.

In order to obtain the actual contents of BiPO$_4$, mpg-C$_3$N$_4$, and (NH$_4$)$_2$SiF$_6$ in the mpg-C$_3$N$_4$/BiPO$_4$ composites, Rietveld refinement of XRD patterns was performed using the MAUD and FindIt program [51], and the results were summarized in Table 1. It could be seen that there were 92.3% mpg-C$_3$N$_4$ and 7.7% (NH$_4$)$_2$SiF$_6$ in mpg-C$_3$N$_4$. With increasing the mass ratio of mpg-C$_3$N$_4$ and BiPO$_4$ from 4:6 to 9.9:0.1, the contents of mpg-C$_3$N$_4$ and (NH$_4$)$_2$SiF$_6$ were increased gradually, while the content of BiPO$_4$ was decreased gradually. The space groups of BiPO$_4$, mpg-C$_3$N$_4$ and (NH$_4$)$_2$SiF$_6$ were P21/c:b2, P-6m2 and Fm-3m, respectively.

The morphology and microstructure of mpg-C$_3$N$_4$, BiPO$_4$ and 9.5CN/BPO observed by TEM were exhibited in Fig. 2. As shown in Fig. 2a, mpg-C$_3$N$_4$ exhibited a mesoporous structure with pore sizes ranging from 5 nm to 60 nm. Moreover, some irregular nanorods were observed with mpg-C$_3$N$_4$. The HR-TEM image of mpg-C$_3$N$_4$ was also displayed (Fig. 2b). The phase with the clear lattice fringes (0.483 nm) corresponded to the (111) crystallographic planes of (NH$_4$)$_2$SiF$_6$, while the phase without fringes was assigned to mpg-C$_3$N$_4$. Fig. 2c demonstrated that BiPO$_4$ was mainly composed of regular nanorods with diameters from 80 to 620 nm and lengths ranging from 0.2 to 1.1 μm. The HR-TEM image in Fig. 2d clearly
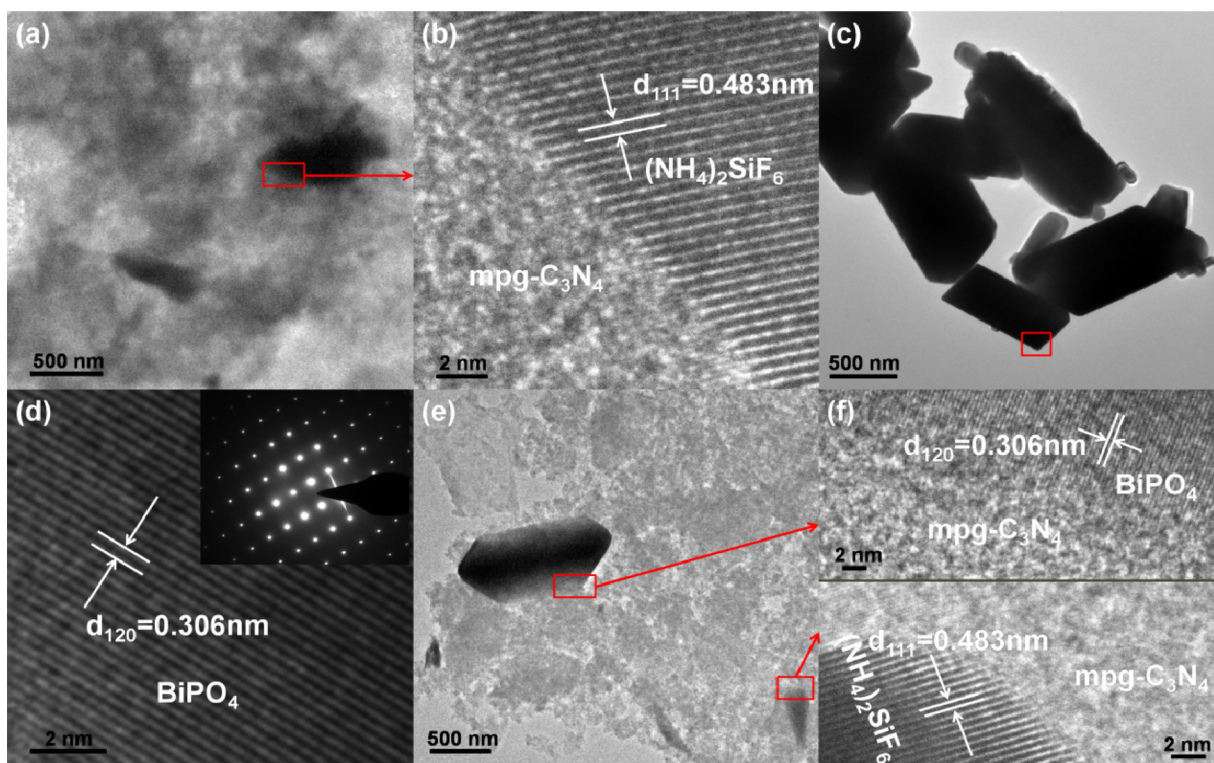
Fig. 2. TEM images of (a, b) mpg-C_3N_4, (c, d) $BiPO_4$ and (e, f) 9.5CN/0.5BPO.

Table 1
Rietveld refined contents of $BiPO_4$, mpg-C_3N_4 and $(NH_4)_2SiF_6$ in mpg-C_3N_4/$BiPO_4$ composites.

Sample	R_w	Symmetry	Space group
$BiPO_4$	13.87%	Monoclinic $BiPO_4$ (100%)	P21/c:b2
4CN/6BPO	14.79%	Monoclinic $BiPO_4$ (60%)	P21/c:b2
		Hexagonal mpg-C_3N_4 (36.6%)	P-6m2
		Cubic $(NH_4)_2SiF_6$ (3.4%)	Fm-3m
5CN/5BPO	14.21%	Monoclinic $BiPO_4$ (50.2%)	P21/c:b2
		Hexagonal mpg-C_3N_4 (45.7%)	P-6m2
		Cubic $(NH_4)_2SiF_6$ (4.1%)	Fm-3m
7CN/3BPO	15.16%	Monoclinic $BiPO_4$ (29.3%)	P21/c:b2
		Hexagonal mpg-C_3N_4 (64.9%)	P-6m2
		Cubic $(NH_4)_2SiF_6$ (5.8%)	Fm-3m
9CN/1BPO	14.93%	Monoclinic $BiPO_4$ (10.6%)	P21/c:b2
		Hexagonal mpg-C_3N_4 (83.0%)	P-6m2
		Cubic $(NH_4)_2SiF_6$ (6.4%)	Fm-3m
9.5CN/0.5BPO	15.07%	Monoclinic $BiPO_4$ (5.8%)	P21/c:b2
		Hexagonal mpg-C_3N_4 (87.1%)	P-6m2
		Cubic $(NH_4)_2SiF_6$ (7.1%)	Fm-3m
9.9CN/0.1BPO	13.96%	Monoclinic $BiPO_4$ (1.3%)	P21/c:b2
		Hexagonal mpg-C_3N_4 (91.2%)	P-6m2
		Cubic $(NH_4)_2SiF_6$ (7.5%)	Fm-3m
mpg-C_3N_4	10.46%	Hexagonal mpg-C_3N_4 (92.3%)	P-6m2
		Cubic $(NH_4)_2SiF_6$ (7.7%)	Fm-3m

revealed that the interplanar spacing of 0.306 nm corresponded to the (120) plane of monoclinic $BiPO_4$. From the inset in Fig. 2d, the selected-area electron diffraction of a single nanorod exhibited a single crystalline structure. Fig. 2e was the TEM image of 9.5CN/0.5BPO, it could be clearly seen that the $BiPO_4$ nanorod was anchored on the surface of mpg-C_3N_4 nanosheets, and an ambiguous interface between mpg-C_3N_4 and $BiPO_4$ was observed. This demonstrated the formation of the mpg-C_3N_4/$BiPO_4$ core-shell heterostructure, which was favorable for the charge transfer

[52]. Therefore, the mpg-C_3N_4/$BiPO_4$ composites were expected to exhibit enhanced photocatalytic activity. Meanwhile, the irregular nanorods still existed in 9.5CN/0.5BPO. Two clear lattice fringes could be observed in the HR-TEM image of 9.5CN/0.5BPO (Fig. 2f). The lattice spacing of 0.306 nm corresponded to the (120) lattice plane of $BiPO_4$ (Fig. 2f upper part). The observed lattice fringe with the interval of 0.483 nm corresponded to the (110) crystallographic plane of $(NH_4)_2SiF_6$ (Fig. 2f bottom part). Likewise, the lattice fringe of mpg-C_3N_4 was difficult to be found. Furthermore, the Zeta potentials of mpg-C_3N_4 and $BiPO_4$ measured in ethanol were −2.98 mV and 4.32 mV, respectively, which indicated that mpg-C_3N_4 and $BiPO_4$ possessed opposite charges on their surfaces. Therefore, the close interface could be formed by the electrostatic interaction between mpg-C_3N_4 and $BiPO_4$.

The composition information and chemical bonding of mpg-C_3N_4, $BiPO_4$ and mpg-C_3N_4/$BiPO_4$ composites with different mass ratios were investigated by FT-IR (Fig. 3a). In the FT-IR spectrum of mpg-C_3N_4, the absorption peak at around 810 cm^{-1} could be attributed to the characteristic breathing mode of triazine units [53]. The characteristic peaks at 1250, 1325, 1403, 1463, 1572 and 1639 cm^{-1} observed in mpg-C_3N_4 corresponded to the typical stretching modes of CN heterocycles [54]. The broad peak at around 3000–3600 cm^{-1} was indicative of the stretching vibration of N—H bonds rather than the O—H stretching associated with adsorbed water [55], considering that no peak was observed even on the pure $BiPO_4$. In the FT-IR spectrum of $BiPO_4$, the peaks at 530, 554 and 605 cm^{-1} were associated with the bending vibration of O—P—O linkages. The peaks at 959, 1005 and 1075 cm^{-1} were attributed to the υ_3 asymmetric stretching vibration of P-O bonds, while the peak at 929 cm^{-1} was assigned to the corresponding υ_1 symmetric vibration [56]. The characteristic absorption peaks of mpg-C_3N_4 were still present in the FT-IR spectra of mpg-C_3N_4/$BiPO_4$ composites, suggesting that no structural change of mpg-C_3N_4 occurred during the hybridization process, which was consistent with the XRD results. With increasing the mass ratio of mpg-C_3N_4 and $BiPO_4$
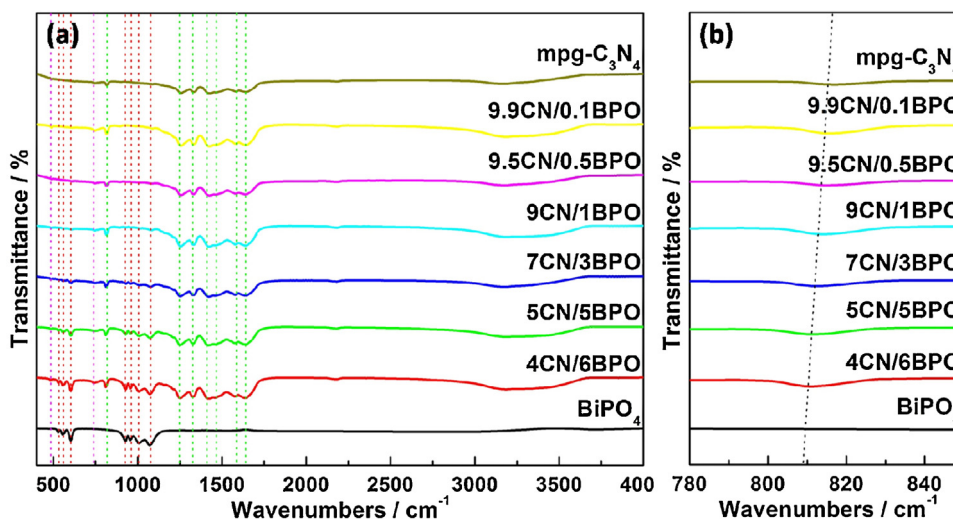
Fig. 3. FT-IR spectra of mpg-C_3N_4, $BiPO_4$ and mpg-C_3N_4/$BiPO_4$ composites with different mass ratios.

from 4:6 to 9.9:0.1, the intensities of characteristic peaks representing $BiPO_4$ gradually decreased, which might be attributed to the increased mpg-C_3N_4 content in the mpg-C_3N_4/$BiPO_4$ composites. Additionally, another two peaks at 480 and 733 cm^{-1} corresponded to the characteristic peaks of SiF_6^{2-} ions. It was noteworthy that the characteristic vibration peaks of NH_4^+ ions could not be found in the FT-IR spectra of mpg-C_3N_4 and mpg-C_3N_4/$BiPO_4$ composites. The likely reason might be ascribed to the fact that these peaks, which were reported to occur at 1401 cm^{-1} [57], were close to the FT-IR peak at 1403 cm^{-1} of mpg-C_3N_4, which made it difficult to differentiate NH_4^+ ions from the FT-IR spectra. Nevertheless, from the narrow scan spectra (Fig. 3b), it could be seen that the characteristic peak at 810 cm^{-1} was slightly shifted to a lower wavenumber with increasing the content of $BiPO_4$, which could be attributed to the strong electrostatic interaction between mpg-C_3N_4 and $BiPO_4$. This conclusion could be further confirmed by the XPS analysis.

To further investigate the interaction between mpg-C_3N_4 and $BiPO_4$, XPS analysis was performed to identify the chemical states of mpg-C_3N_4, $BiPO_4$ and 9.5CN/0.5BPO (Fig. 4). The peak positions in all of the XPS spectra were calibrated with C 1s at 284.6 eV. The XPS survey spectra (Fig. 4a) suggested that the 9.5CN/0.5BPO was primarily composed of Bi, P, O, C, N, Si and F elements, further confirming the co-existence of $BiPO_4$, mpg-C_3N_4 and $(NH_4)_2SiF$ in the composite. High-resolution XPS spectra of Bi 4f, P 2p, O 1s, C 1s and N 1s were shown in Fig. 4b–f. In the Bi 4f spectra (Fig. 4b), peaks at 159.9 eV and 165.1 eV for $BiPO_4$ were ascribed to Bi $4f_{7/2}$ and Bi $4f_{5/2}$ of Bi^{3+}, respectively [58]. However, those peaks in the spectrum of 9.5CN/0.5BPO shifted to 160.1 eV and 165.3 eV, respectively, which were 0.2 eV higher than those of $BiPO_4$. In the P 2p spectrum of $BiPO_4$, the peak at 133.2 eV was attributed to P of PO_4^{3-} [59]. Correspondingly, this P 2p peak in the 9.5CN/0.5BPO also displayed a slight shift compared to $BiPO_4$. A similar phenomenon was also observed in the O 1s spectra (Fig. 4d). The binding energy of O 1s in 9.5CN/0.5BPO could be observed at 531.4 eV, showing a positive shift compared with that of $BiPO_4$ (531.0 eV) [10]. These shifts (Fig. 4b–d) in XPS measurement could be ascribed to the chemical environment change arising from the strong interaction between mpg-C_3N_4 and $BiPO_4$ [60], which further confirmed the existence of electrostatic force between mpg-C_3N_4 and $BiPO_4$ in the heterojunction. The XPS spectra of C 1s for mpg-C_3N_4 and 9.5CN/0.5BPO could be observed in Fig. 4e. The binding energy centered at 284.6 eV was assigned to the adventitious hydrocarbon from the XPS instrument itself, whereas the other C 1s peak occurred at 288.3 eV was ascribed to the sp^2-hybridized carbon in N-containing aro-

matic ring (N—C=N) [61]. The broad N 1s peak in the spectrum of mpg-C_3N_4 was deconvoluted into four Gaussian-Lorenzian peaks centered at 398.7 eV, 400.2 eV, 401.3 eV and 404.3 eV, which could be attributed to triazine rings (C=N—C), tertiary nitrogen (N—$(C)_3$), amino functions (N—H), as well as the charging effects, respectively, in accordance with the reported results [62]. As expected, the peaks of N 1s for 9.5CN/0.5BPO shifted toward lower binding energies relative to mpg-C_3N_4. Moreover, it could be seen that the Bi 4f, P 2p, and O 1s peak intensity in 9.5CN/0.5BPO was weaker than that of $BiPO_4$, which could be due to the lower content of $BiPO_4$ in the 9.5CN/0.5BPO, which was consistent with the TEM. Based on the above TEM, FT-IR and XPS results, we concluded that there was strong electrostatic interaction between mpg-C_3N_4 and $BiPO_4$, which could promote the transfer of photogenerated electron-hole pairs and thus enhance the photocatalytic activity of mpg-C_3N_4/$BiPO_4$ composites [63].

The N_2 adsorption-desorption isotherms and the corresponding pore size distribution curves (inset) of mpg-C_3N_4 and 9.5CN/0.5BPO were in Fig. 5. It could be seen that both isotherms were of type IV according to the IUPAC classification with a H3 hysteresis loop observed in the range of 0.55–1.00 P/P_0, confirming the presence of mesopores (2–50 nm) [64]. This also indicated that the addition of $BiPO_4$ did not significantly block or alter the pore structure of mpg-C_3N_4 [65]. In addition, the isotherms of mpg-C_3N_4 and 9.5CN/0.5BPO showed high adsorption at the high relative pressure (P/P_0) of approaching 1.0, suggesting the coexistence of large mesopores and macropores, which were resulted from the aggregation of nanosheets [66]. The pore size distributions (inset in Fig. 5) showed that the pores of mpg-C_3N_4 and 9.5CN/0.5BPO were mainly distributed in the range of 3–70 nm, further demonstrating the existence of mesopores and macropores. The total pore volume and average pore diameter obtained for mpg-C_3N_4 were 0.66 cm^3g^{-1} and 16.7 nm, respectively. These values were slightly higher than the corresponding values, 0.63 cm^3g^{-1} and 13.0 nm, estimated for 9.5CN/0.5BPO. The BET surface area of 9.5CN/0.5 BPO was found to be 195.4 m^2g^{-1}, which was slightly larger than the value for mpg-C_3N_4 (158.2 m^2g^{-1}). The high specific surface area was likely to contribute to the improvement of photocatalytic activity [58]. In addition, the BET specific surface areas were calculated to be 12.0 m^2g^{-1} and 24.2 m^2g^{-1} for g-C_3N_4 and 9.5GCN/0.5BPO, respectively.

UV-vis diffuse reflectance spectroscopy was utilized to investigate the optical properties of mpg-C_3N_4, $BiPO_4$ and mpg-C_3N_4/$BiPO_4$ composites. As illustrated in Fig. 6a, mpg-C_3N_4 showed
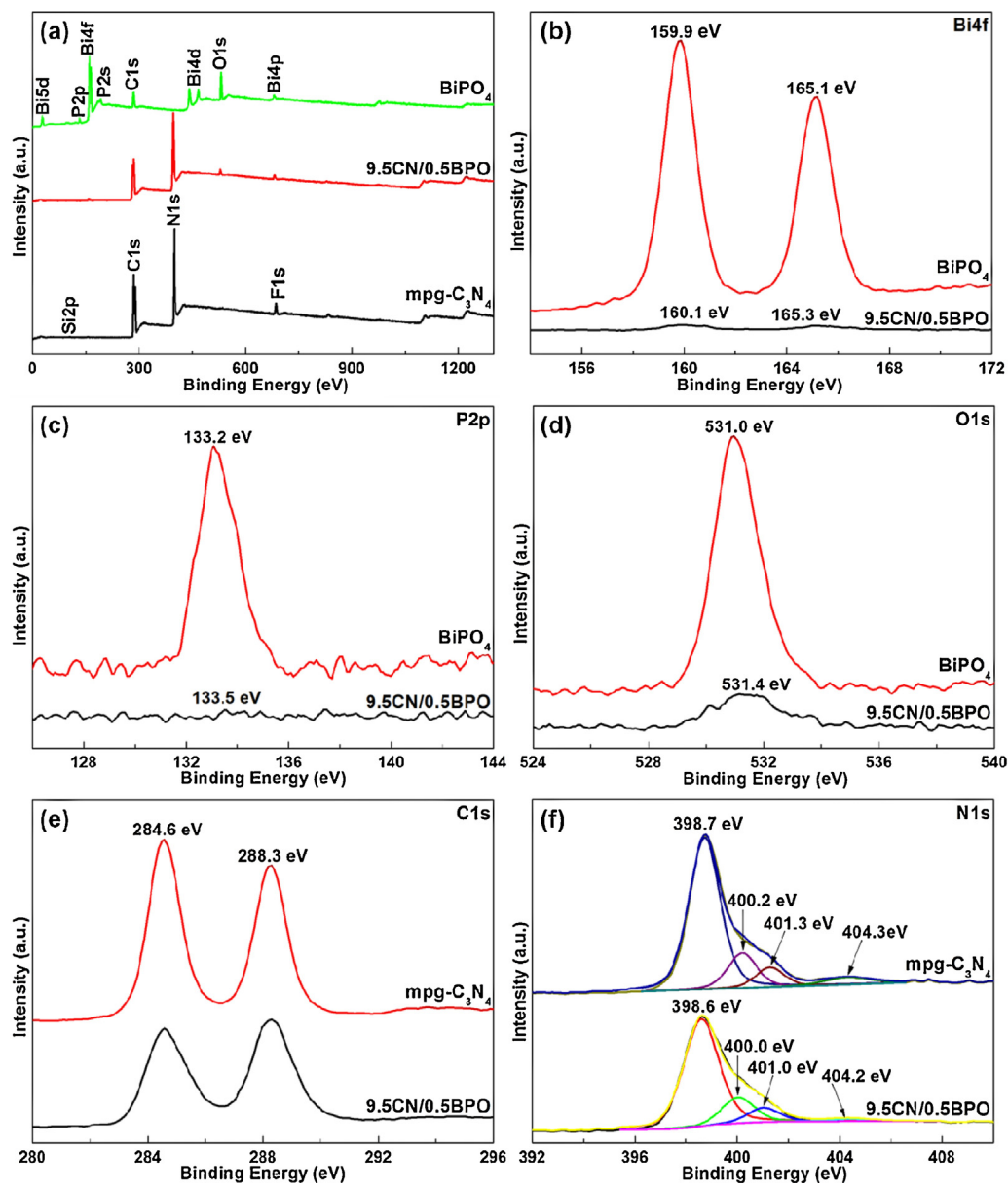
Fig. 4. (a) XPS survey spectra of mpg-C_3N_4, $BiPO_4$ and 9.5CN/0.5BPO; XPS spectra of $BiPO_4$ and 9.5CN/0.5BPO: (b) Bi 4f, (c) P 2p and O 1s; XPS spectra of mpg-C_3N_4 and 9.5CN/0.5BPO: (e) C 1s and (f) N 1s.

a wider photoabsorption from UV light to visible light with an absorption edge at around 463 nm. Nevertheless, $BiPO_4$ only responded to the UV light, whose absorption edge was about 310 nm. It was notable that the optical absorption intensity of mpg-C_3N_4 in UV-light region was higher than that of $BiPO_4$. Compared with pure $BiPO_4$, the optical absorption edges of the mpg-C_3N_4/$BiPO_4$ composites were gradually red-shifted with increasing the mass ratio of mpg-C_3N_4 and $BiPO_4$ from 4:6 to 9.9:0.1 (inset in Fig. 6a), indicating that all the mpg-C_3N_4/$BiPO_4$ composites possessed visible light response. Furthermore, the band gap energies of mpg-C_3N_4, $BiPO_4$ and \\mpg-C_3N_4/$BiPO_4$ composites could be estimated by Kubelka-Munk transformation:

$$\alpha h\nu = A(h\nu - E_g)^{n/2}$$

where α represented the absorption coefficient, h was Planck constant, ν was the light frequency, E_g was the band gap energy, A was a proportionality constant and n depended on the optical transition type of a semiconductor (n = 1 for direct transition and n = 4

for indirect transition) [1]. As previous literature reported, the n values of $BiPO_4$ [67] and mpg-C_3N_4 [19] were 4 and 1, respectively. The band gaps (E_g) of the resulting photocatalysts could be estimated from the plots of $(\alpha h\nu)^{n/2}$ versus $h\nu$. As shown in Fig. 6b, the energy band gaps (E_g) of $BiPO_4$, 4CN/6BPO, 5CN/5BPO, 7CN/3BPO, 9CN/1BPO, 9.5CN/0.5BPO, 9.9CN/0.1BPO and mpg-C_3N_4 were estimated to be 3.83 eV, 2.86 eV, 2.85 eV, 2.84 eV, 2.83 eV, 2.82 eV, 2.81 eV and 2.81 eV, respectively.

3.2. Photocatalytic activity

The photocatalytic activity of mpg-C_3N_4/$BiPO_4$ composites with different mass ratios was evaluated by RhB degradation under visible ($\lambda > 420$ nm), UV and solar light irradiation, respectively (Fig. 7). The degradation process was fit to pseudo- first-order kinetics in which the value of apparent reaction rate constant k was equal to the corresponding slope of the fitting line [68]. Under visible light irradiation (Fig. 7a), the photolysis of RhB could be negli-
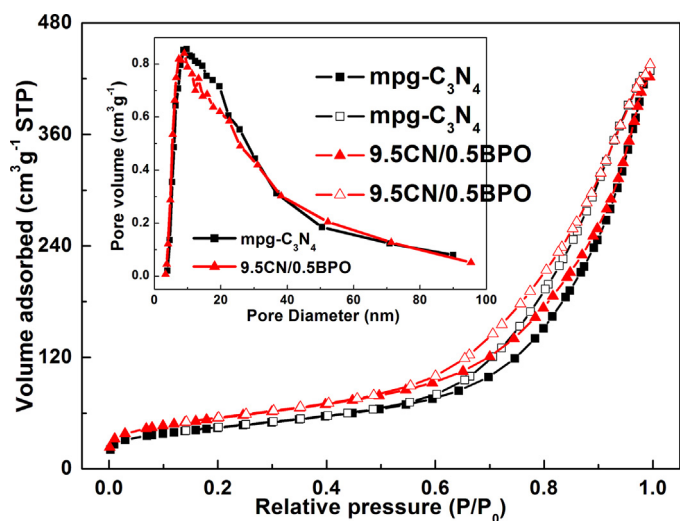
Fig. 5. N_2 adsorption-desorption isotherms and the corresponding pore size distribution curves (inset) of mpg-C_3N_4 and 9.5CN/0.5BPO. Closed symbols, adsorption; open symbols, desorption.

gible on the basis of the result of blank experiment. Pure $BiPO_4$ played no role in degrading RhB due to its large band gap energy. Moreover, the degradation rate of RhB over mpg-C_3N_4 reached 84.2% in 30 min. As expected, the mpg-C_3N_4/$BiPO_4$ composites exhibited higher photocatalytic activity than mpg-C_3N_4, except for the 4CN/6BPO. The photocatalytic activity was increased gradually with increasing mass ratios of mpg-C_3N_4 and $BiPO_4$ from 4:6 to 9.5:0.5. When the ratio of mpg-C_3N_4/$BiPO_4$ was 9.5:0.5, the highest photocatalytic activity of mpg-C_3N_4/$BiPO_4$ was obtained. The 9.5CN/0.5BPO could degrade 92.3% of RhB in 30 min with a reaction rate constant of 0.08393 min^{-1}, which was about 1.3 times as high as that of mpg-C_3N_4 (0.06237 min^{-1}) (Fig. 7b), and much superior than that of the previous reports [5,45–47]. Nevertheless, with the further increase of mass ratio, the photocatalytic activity of 9.9CN/0.1BPO decreased. In contrast to the hybrid composites, the photocatalytic activity of the mechanically mixed 9.5MCN/0.1BPO was slightly higher than that of mpg-C_3N_4, but much lower than that of 9.5CN/0.5BPO.

In the case of UV light irradiation (Fig. 7c), it could be observed that the photocatalytic activity of mpg-C_3N_4 was much higher than that of commercial TiO_2 (P25) and $BiPO_4$. Similar to the visible-light catalytic activity, the UV-light catalytic activity of mpg-C_3N_4/$BiPO_4$ composites was enhanced. Among the hybrid composites, 9.5CN/0.5BPO still showed the best photocatalytic activity. Surprisingly, it took only 6 min of UV light irradiation for

the complete degradation of RhB over 9.5CN/0.5BPO (94.3%). The degradation rate was determined to be 0.48469 min^{-1} (Fig. 7d), which was approximately 4.2 times higher than that of $BiPO_4$ and 1.5 times larger than that of mpg-C_3N_4. In addition, the mechanical mixture of mpg-C_3N_4 and $BiPO_4$ with a 9.5:0.5 mass ratio showed lower photocatalytic activity than that of 9.5CN/0.5BPO. The photocatalytic activity of mpg-C_3N_4/$BiPO_4$ composites was also detected under solar light irradiation (Fig. 7e), the order of the photocatalytic activity was the same as that obtained under visible light irradiation. However, the degradation rate of mpg-C_3N_4/$BiPO_4$ under sun light irradiation was much larger than that under visible light irradiation, which might be caused by $BiPO_4$ that could be excited by UV light in the sun light. The 9.5CN/0.5BPO also exhibited the highest photocatalytic activity among all composites, which could almost degrade RhB completely within 24 min with a reaction rate constant of 0.14082 min^{-1}, which was about 1.2 times as high as that of mpg-C_3N_4 (0.11426 min^{-1}) (Fig. 7f). For the mechanically blended 9.5MCN/0.1BPO, its photocatalytic activity was lower than that of 9.5CN/0.1BPO. According to the above results, we inferred that the interaction between mpg-C_3N_4 and $BiPO_4$ facilitated the formation of mpg-C_3N_4/$BiPO_4$ heterostructure and generated a novel and highly efficiency photocatalyst [69].

Fig. S2 exhibited the photocatalytic degradation of RhB by 9.5GCN/0.5BPO and 9.5CN/0.5BPO under visible and UV light irradiation. It was obvious that the 9.5CN/0.5BPO showed much higher photocatalytic activity than 9.5GCN/0.5BPO. The BET specific surface area of 9.5CN/0.5BPO was 195.4 m^{2}g^{-1}, which was about 8.1 times of the 9.5GCN/0.5BPO (24.2 m^{2}g^{-1}). Thus 9.5CN/0.5BPO could provide more active sites for photocatalytic reaction, resulting in an enhanced photocatalytic activity.

Moreover, the changes in the TOC reflected the degree of mineralization of an organic molecule during testing period [70]. From these results, it could be observed that, after visible light irradiation for 40 min, the mineralization efficiencies of $BiPO_4$, mpg-C_3N_4 and 9.5CN/0.5BPO were calculated to be 1.9%, 39.55% and 48.68%, respectively (Fig. 8a). On the other hand, after UV light irradiation for 8 min, the mineralization efficiencies of P25, $BiPO_4$, mpg-C_3N_4 and 9.5CN/0.5BPO were evaluated to be 9.21%, 13.47%, 57.42% and 64.27%, separately (Fig. 8b). The above results indicated that the 9.5CN/0.5BPO could not only degrade RhB but also mineralize it under visible and UV light irradiation, working as an efficient photocatalyst to degrade dye pollutants in water.

The photocatalytic degradation products of RhB by 9.5CN/0.5BPO under visible and UV light irradiation were examined by HPLC, as shown in Fig. 9. The HPLC chromatograms of RhB degradation were similar with the previous results of Zhang's group [71]. It was well-reported that the degradation of RhB mainly included two competitive processes: N-deethylation and
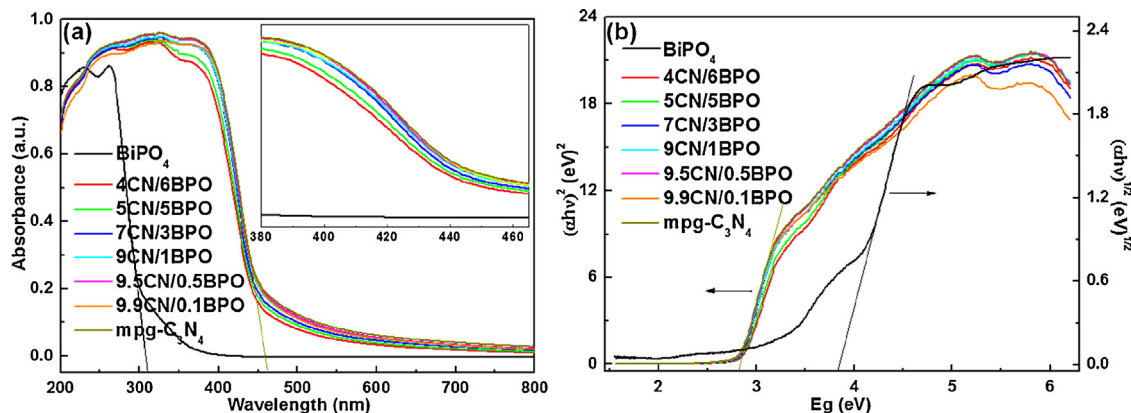

Fig. 6. UV–vis diffuse reflectance spectra (a) and the corresponding Kubelka-Munk transformed reflectance spectra (b) of mpg-C_3N_4, $BiPO_4$ and mpg-C_3N_4/$BiPO_4$ composites.
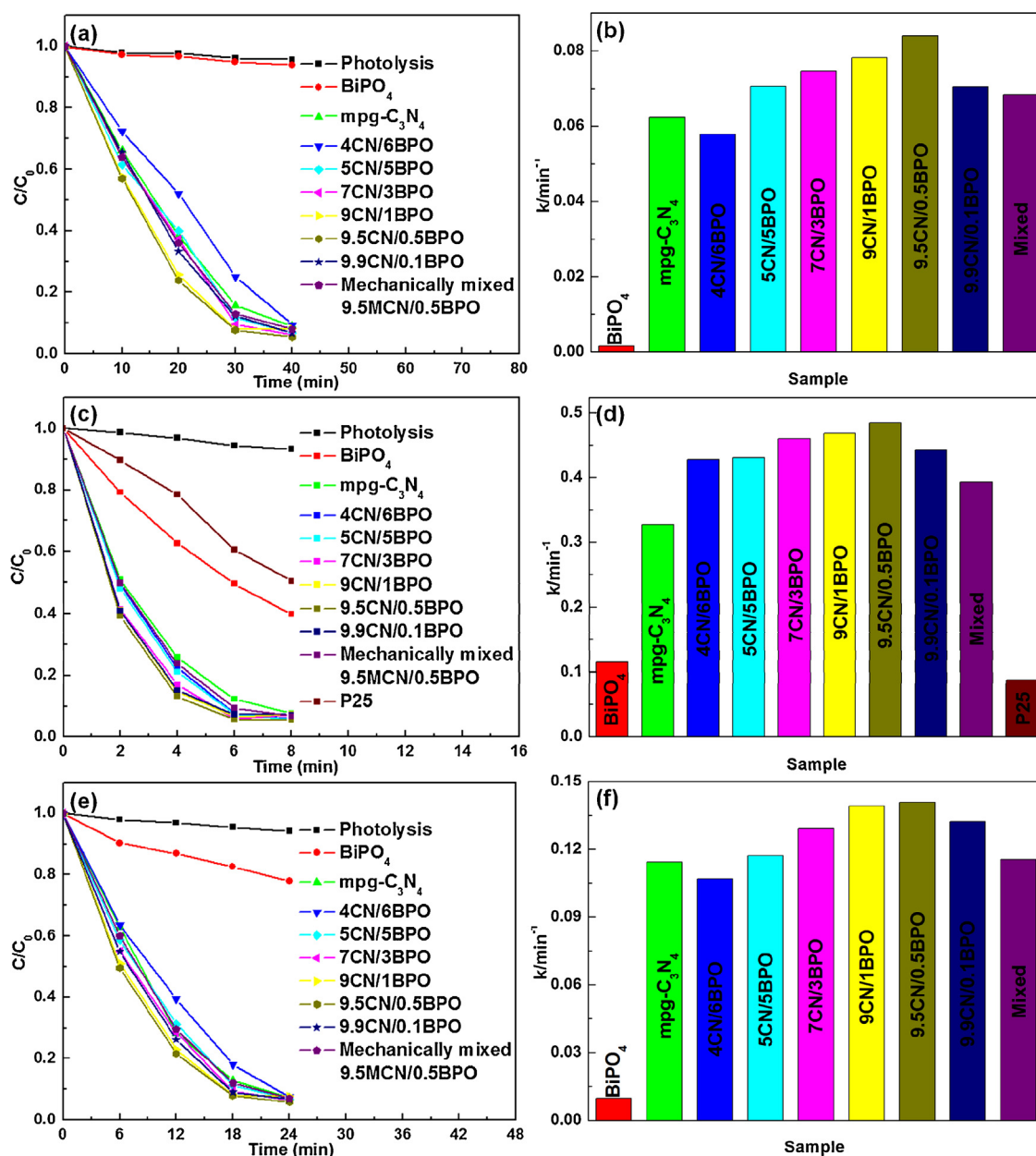
Fig. 7. (a) Photocatalytic degradation of RhB and (b) the corresponding rate constant k values of $BiPO_4$, mpg-C_3N_4 and mpg-C_3N_4/$BiPO_4$ composites under visible light irradiation; (c) photocatalytic degradation of RhB and (d) the corresponding rate constant k values of P25, $BiPO_4$, mpg-C_3N_4 and mpg-C_3N_4/$BiPO_4$ composites under UV light irradiation; (e) photocatalytic degradation of RhB and (f) the corresponding rate constant k values of $BiPO_4$, mpg-C_3N_4 and mpg-C_3N_4/$BiPO_4$ composites under solar light irradiation.

Fig. 8. TOC removal of RhB over the samples: (a) under visible light irradiation for 40 min and (b) under UV light irradiation for 8 min.
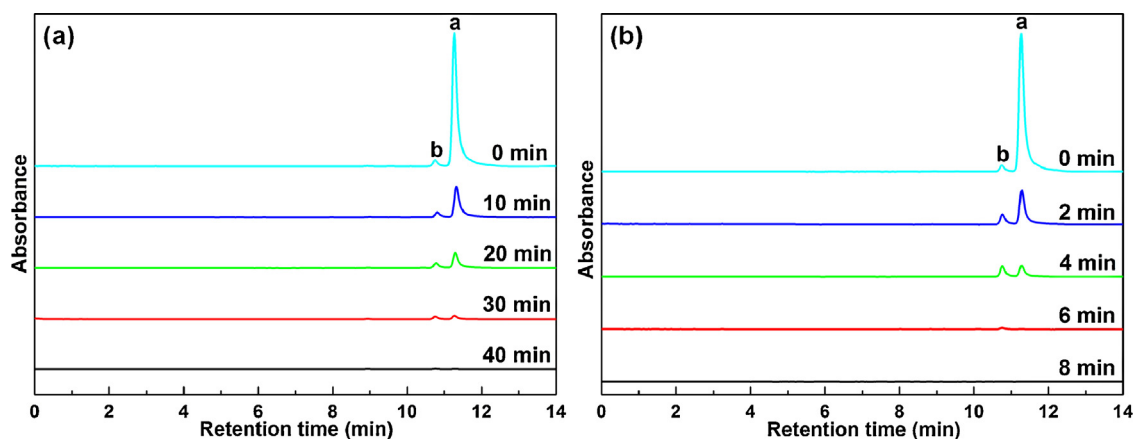
Fig. 9. HPLC chromatograms of RhB photodegradation over 9.5CN/0.5BPO under (a) visible and (b) UV light irradiation.

Table 2
The concentration of Bi ions in the solution after the photocatalytic operation.

Sample	Bi ions concentration (ppm)
9.5CN/0.5BPO (visible)	0.17
9.5CN/0.5BPO (UV)	0.23
BiPO$_4$ (UV)	2.54

the decomposition of the conjugated chromophore structure [72,73]. Under visible light irradiation (Fig. 9a), it was found that only one intermediate was observed (peak b) during the degradation of RhB, namely, *N,N*-diethyl-*N*′-ethylrhodamine (DER), which was identified based on the reported literature [74]. This phenomenon demonstrated that N-deethylation pathway was depressed. With the rapid decrease of RhB (peak a), the concentration of DER species was increased slightly and then gradually decreased. Similarly, the intense peak of RhB disappeared quickly after UV light irradiation for 6 min, and the concentration of DER species increased and subsequently decreased with further irradiation (Fig. 9b). The above results indicated that the destruction of the conjugated structure of RhB would be the major process [75].

The stability of mpg-C$_3$N$_4$/BiPO$_4$ composites was investigated by performing recycling experiments with 9.5CN/0.5BPO under visible light irradiation. As can be seen from Fig. 10a, the 9.5CN/0.5BPO did not exhibit significant loss of photocatalytic activity after four consecutive recycling runs, illustrating its excellent stability under visible light irradiation. A slight decrease of photocatalytic activity might be from the loss of the photocatalyst by centrifugation. Furthermore, the XRD pattern of 9.5CN/0.5BPO after 4th run cycle was shown in Fig. 10b. It could be clearly observed that the (111), (400) and (511) diffraction peaks of (NH$_4$)$_2$SiF$_6$ were disappeared in the XRD pattern of 9.5CN/0.5BPO after the 4th run cycle, demonstrating that the mpg-C$_3$N$_4$ was indeed not thoroughly washed with distilled water and absolute ethyl alcohol. These data also indicated that the (NH$_4$)$_2$SiF$_6$ as an impurity had no effect on the photocatalytic activity of 9.5CN/0.5BPO.

The concentration of Bi ions in the solution after the photocatalytic operation was determined by ICP-OES analysis. As shown in Table 2, for 9.5CN/0.5BPO, the concentrations of Bi ions in the solution after visible and UV light irradiation were 0.17 ppm and 0.23 ppm, respectively. For BiPO$_4$, the concentration of Bi ions in the solution after UV light irradiation was 2.54 ppm. For 9.5CN/0.5BPO and BiPO$_4$, after calculation, we could know that the initial concentrations of Bi ions in the solution before the photocatalytic reaction were 1000 ppm and 50 ppm, respectively. By comparison, it was found that the concentration of Bi ions in the solution after the photocatalytic reaction was extremely low, indicating that BiPO$_4$ possessed high stability, which was in accord with the reported

in the literature [6]. As for the extremely small amount of Bi ions, it might be because the extremely small amount of BiPO$_4$ powders still existed in the solution after centrifuge and filtering. So when the aerosol sample entered into the plasma flame, the BiPO$_4$ molecules would be decomposed into Bi^{3+} and PO$_4$$^{3-}$. Therefore, the extremely small amount of Bi ions was detected in our experiments. These results further demonstrated that the as-prepared photocatalysts were sufficiently stable in the degradation of RhB.

To investigate the universal application of mpg-C$_3$N$_4$/BiPO$_4$ composites, 9.5CN/0.5BPO was further evaluated for the photocatalytic degradation of MO and phenol in aqueous solution, where MO was an anionic dye, while phenol was neutral and persistent due to its stable benzene ring structure [76]. Fig. 11 displayed the comparison of 9.5CN/0.5BPO on the photocatalytic degradation of RhB, MO and phenol aqueous solution under visible and UV light irradiation. From these results, it could be seen that, after visible light irradiation for 40 min (Fig. 11a), the degradation rates of RhB, MO and phenol over 9.5CN/0.5BPO were close to 94.6%, 86.6% and 64.7%, separately. On the other hand, after UV light irradiation for 8 min (Fig. 11b), the degradation rates of RhB, MO and phenol over 9.5CN/0.5BPO were about 94.4%, 89.5% and 74.4%, respectively. The above results suggested that mpg-C$_3$N$_4$/BiPO$_4$ composites had no-selectivity and could effectively degrade three organic dyes [77].

3.3. Photocatalytic mechanism

In order to further get insights into the photocatalytic mechanism, the active species generated during the reaction process were detected through the trapping experiments of radicals over 9.5CN/0.5BPO under visible and UV light irradiation (Fig. 12). *tert*-Butyl alcohol (TBA), disodium ethylenediaminetetraacetate (EDTA-2Na) and benzoquinone (BQ) were used as hydroxyl radicals (•OH), holes (h$^+$) and superoxide radicals (•O$_2$$^-$) scavengers, respectively [78]. Under visible light irradiation (Fig. 12a), for 9.5CN/0.5BPO (94.6%), the addition of TBA just slightly depressed the degradation of RhB (91.9%), suggesting that •OH was a minor active species in the photocatalytic process. Moreover, it could be observed that the addition of BQ inhibited the degradation of RhB almost completely (1.7%), indicating that •O$_2$$^-$ was the predominant reactive species in the photocatalytic system. The degradation rate of RhB was also reduced largely (71.9%) after the addition of EDTA-2Na, implying that h$^+$ was another main reactive species (after •O$_2$$^-$).

Under UV light irradiation (Fig. 12b), for 9.5CN/0.5BPO (94.4%), it could be seen that the photocatalytic degradation rate was almost inhibited completely with the addition of BQ (1.2%), indicating that dissolved O$_2$ has an obvious effect on the degradation pro-
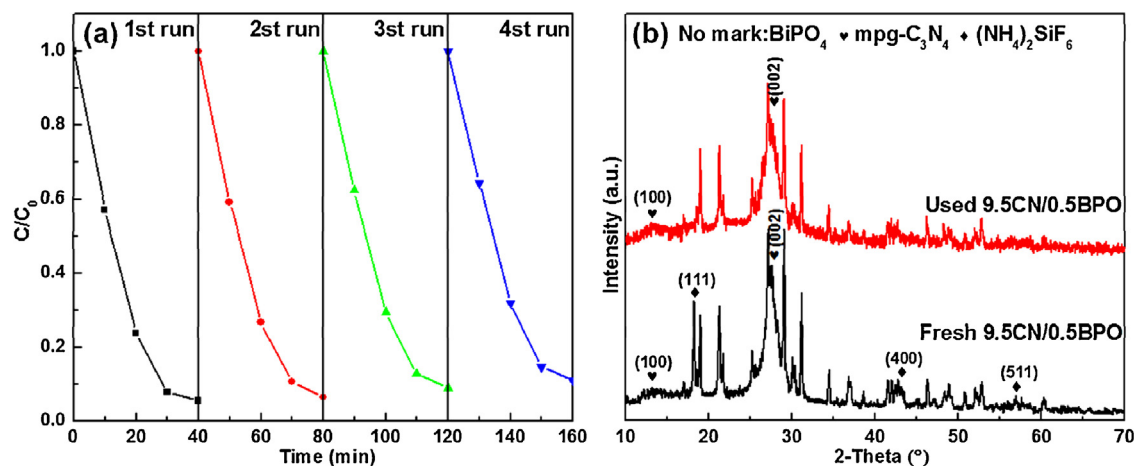
Fig. 10. (a) Cycling runs of 9.5CN/0.5BPO for the degradation of RhB under visible light irradiation; (b) XRD patterns of 9.5CN/0.5BPO before and after 4th run cycle photocatalytic experiments.
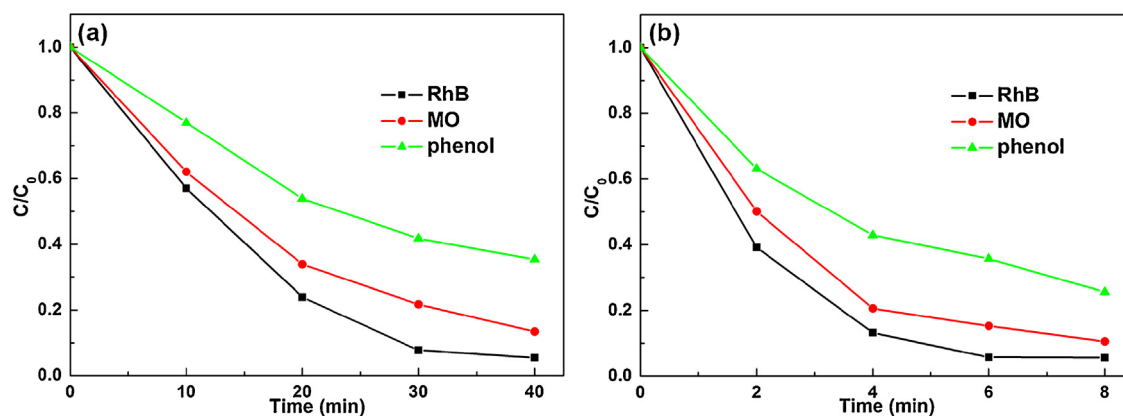

Fig. 11. A comparison of 9.5CN/0.5BPO on the photocatalytic degradation of RhB, MO and phenol aqueous solution under (a) visible and (b) UV light irradiation.
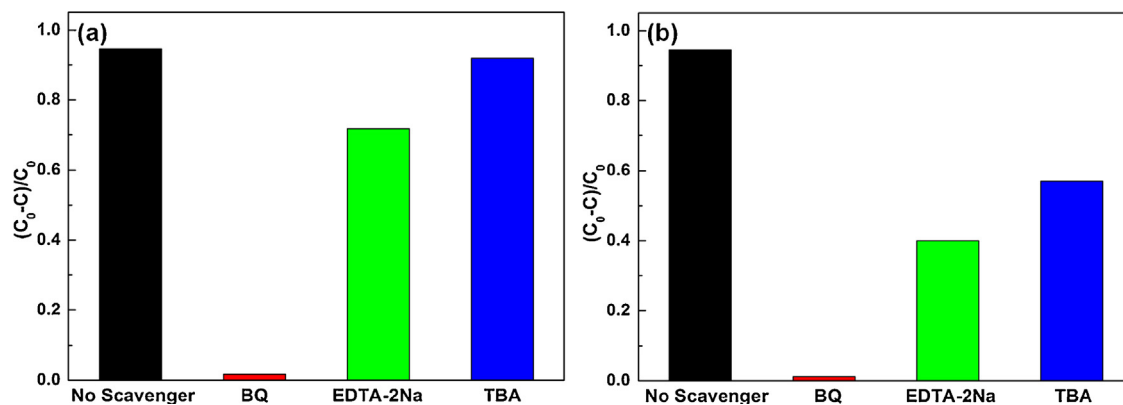

Fig. 12. Effects of different scavengers on the photocatalytic activity of 9.5CN/0.5BPO under (a) visible and (b) UV light irradiation.

cess. Meanwhile, the degradation rate of RhB was also decreased obviously when EDTA-2Na (40.0%) were added. Nevertheless, the photocatalytic degradation of RhB over 9.5CN/0.5BPO could also be suppressed upon the addition of TBA (56.9%). These results revealed that $\cdot$OH was also the active species generated in the mpg-C_3N_4/BiPO$_4$ photocatalytic system besides $\cdot O_2^-$ and h$^+$ in the mpg-C_3N_4/BiPO$_4$ photocatalytic system.

The photocurrent was widely considered as the most efficient evidence to manifest the photogenerated charge separation in the heterojunction photocatalysts [79,80]. Fig. 13 showed the transient photocurrent responses of BiPO$_4$, mpg-C_3N_4, 9.5MCN/0.5BPO and

mpg-C_3N_4/BiPO$_4$ composites under visible and UV light irradiation, respectively. It could be obviously seen that all the samples presented a photocurrent with good reproducibility when samples were irradiated by visible and UV light, which indicated that the electrodes were stable and the photoresponsive phenomenon was entirely reversible. Under visible light irradiation (Fig. 13a), BiPO$_4$ showed almost no photocurrent response because of its large band gap. The photocurrent of the mechanically mixed 9.5MCN/0.1BPO was slightly higher than that of mpg-C_3N_4, but much lower than that of 9.5CN/BPO, suggesting that no interaction or an extremely weak interaction existed between the two
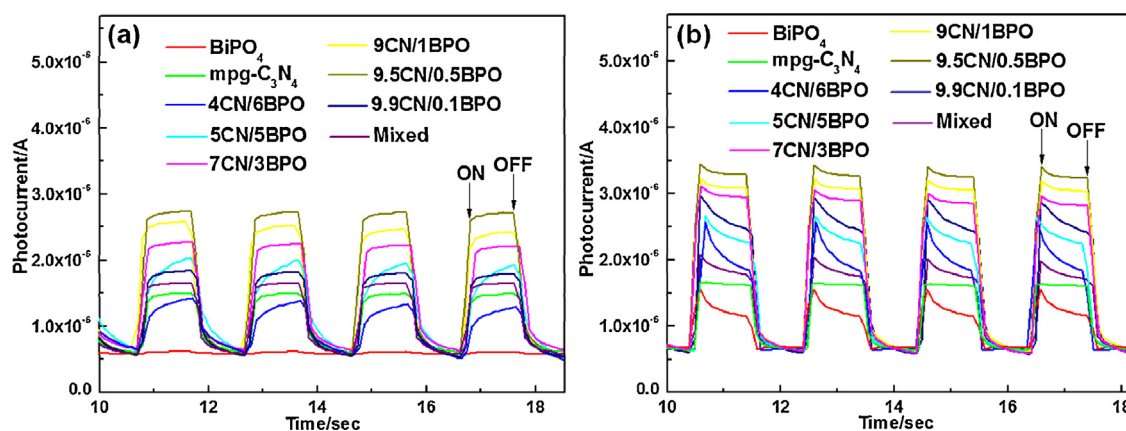
Fig. 13. The transient photocurrent responses of $BiPO_4$, mpg-C_3N_4, 9.5MCN/BPO and mpg-C_3N_4/$BiPO_4$ electrodes with light on-off cycles: (a) under visible light irradiation ($\lambda > 420$ nm, [Na_2SO_4] = 0.1 M) and (b) under UV light irradiation.

semiconductors. It was noted that except for 4CN/6BPO, the photocurrents of mpg-C_3N_4/$BiPO_4$ composites were all higher than that of mpg-C_3N_4. Especially, the 9.5CN/0.5BPO exhibited the highest photocurrent, which was about 2.5 times as high as that of mpg-C_3N_4. These results supported the hypothesis that the formation of mpg-C_3N_4/$BiPO_4$ heterostructure facilitated faster photogenerated charge separation, thus leading to an improved photocurrent [4]. Under UV light irradiation (Fig. 13b), all mpg-C_3N_4/$BiPO_4$ composites showed much higher photocurrent than either mpg-C_3N_4 or $BiPO_4$. Among them, the 9.5CN/0.5BPO also showed the highest photocurrent. Similarly, the mechanically blended 9.5MCN/0.1BPO showed a much lower photocurrent than 9.5CN/0.5BPO. It suggested that a greatly improved photogenerated charge separation occurred at the interface between mpg-C_3N_4 and $BiPO_4$ in the mpg-C_3N_4/$BiPO_4$ composites. It was also found that the order of photocurrent of these electrodes was in accord with that of photocatalytic activity for all samples, which suggested that the interfacial charge transfer for different hybridized photocatalyst was different.

The improved charge separation efficiency in the mpg-C_3N_4/$BiPO_4$ heterojunction was further confirmed by electrochemical impedance spectroscopy (EIS). The EIS Nynquist plots of $BiPO_4$, mpg-C_3N_4 and 9.5CN/0.5BPO before and after visible or UV light irradiation were showed in Fig. 14. It could be observed that there was only one arc on the EIS spectrum, which indicated that only surface charge-transfer was involved in the photocatalytic reaction [81]. Generally, a smaller arc radius on the EIS Nyquist plot meant smaller charge transfer resistance on the electrode surface [82]. Fig. 14 showed that the impedance arc radii of $BiPO_4$, mpg-C_3N_4 and 9.5CN/0.5BPO in the dark were larger than that under visible or UV light irradiation, indicating that there were fewer electrons across the $BiPO_4$, mpg-C_3N_4 and 9.5CN/0.5BPO-electrolyte interface in the dark [83]. We could also see that the arc radius on the EIS Nyquist plot of 9.5CN/0.5BPO was smaller than that of $BiPO_4$ and mpg-C_3N_4 in the cases of visible or UV light irradiation, implying that the separation and transfer rate of photogenerated charge was remarkably improved via an interfacial interaction between mpg-C_3N_4 and $BiPO_4$.

To gain more accurate information, the impedance spectra were fitted through the ZSimpWin software and the fitted impedance parameters were listed in Table 3. The equivalent circuit model (inset of Fig. 14a) included charge-transfer resistance R_{sc}, electrolytic resistance R_d, space charge capacitance C_{sc}, electrochemical double-layer capacitance Q and solution resistance R_L. As showed in Fig. 14, the measured data were the dots, while the solid lines were the fitted results using the provided equivalent circuit. It could be seen that the measured data were fitted very well. From

Table 3, the values of R_{sc} of $BiPO_4$, mpg-C_3N_4 and 9.5CN/0.5BPO were reduced from 111.7 kΩ, 33.18 kΩ and 20.61 kΩ to 99.62 kΩ, 20.09 kΩ and 17.55 kΩ under visible light irradiation, respectively, while the R_{sc} values of $BiPO_4$, mpg-C_3N_4 and 9.5CN/0.5BPO decreased to 90.54 kΩ, 18.94 kΩ and 17.02 kΩ under UV light irradiation, respectively. It was found that the R_{sc} of 9.5CN/0.5BPO was smaller than that of $BiPO_4$ and mpg-C_3N_4 in the cases of visible or UV light irradiation. This fully proved the fastest separation and transfer efficiency of photogenerated charge in the $BiPO_4$/mpg-C_3N_4 composites, in accordance with the photocatalytic activities.

In order to further investigate the intrinsic electronic properties of $BiPO_4$, mpg-C_3N_4 and 9.5CN/BPO, the relation between capacitance of the space charge region and the applied potential was studied by Mott-Schottky (MS) experiments in the dark (Fig. 15) [84]. The positive slope of the plot indicated that these three photocatalysts were n-type semiconductors. According to the intersection point of the potential and linear potential curve, the flat band potential was approximately −0.61 V, −0.89 V and −0.75 V for $BiPO_4$, mpg-C_3N_4 and 9.5CN/BPO, respectively. The conduction band (CB) position was close to the flat band potential [85]. Combined with the values of bandgap (UV-vis DRS results), the estimated valence band (VB) positions were 3.22 V, 1.92 V and 2.07 V for $BiPO_4$, mpg-C_3N_4 and 9.5CN/BPO, respectively. Moreover, the slope of the linear range for 9.5CN/BPO was smaller than that of $BiPO_4$ and mpg-C_3N_4, suggesting higher donor density, which resulted in the faster photodegradation rate [86]. Therefore, the enhanced photocatalytic activity of 9.5CN/BPO compared with $BiPO_4$ and mpg-C_3N_4 could be ascribed to the higher separation efficiency of photogenerated electrons and holes.

On the basis of the above experimental and theoretical calculation results, a possible mechanism for the improved photocatalytic activity of mpg-C_3N_4/$BiPO_4$ heterojunctions in degradation of RhB under visible and UV light irradiation was tentatively proposed by promoting the separation and transfer of photogenerated electrons and holes at the heterostructured interface and schematically illustrated in Fig. 16. Under visible light irradiation (Fig. 16a), $BiPO_4$ could not be excited by visible light because of wider band gap, thus exhibiting a lower photocatalytic activity. Some of the photogenerated electrons in the CB of mpg-C_3N_4 could easily transfer to the CB of $BiPO_4$ through the closely contacted interface because the CB potential of mpg-C_3N_4 (−0.89 eV) was more negative than that of $BiPO_4$ (−0.61 eV). Meanwhile, the photogenerated holes tended to remain in the VB of mpg-C_3N_4. $BiPO_4$ thus served as an electron trap to efficiently facilitate the separation of photoinduced electron-hole pairs, which had an important effect on visible light catalysis activity as evidenced in Fig. 7a. Consequently, the electrons in the CB of both $BiPO_4$ and mpg-C_3N_4 could react with O_2
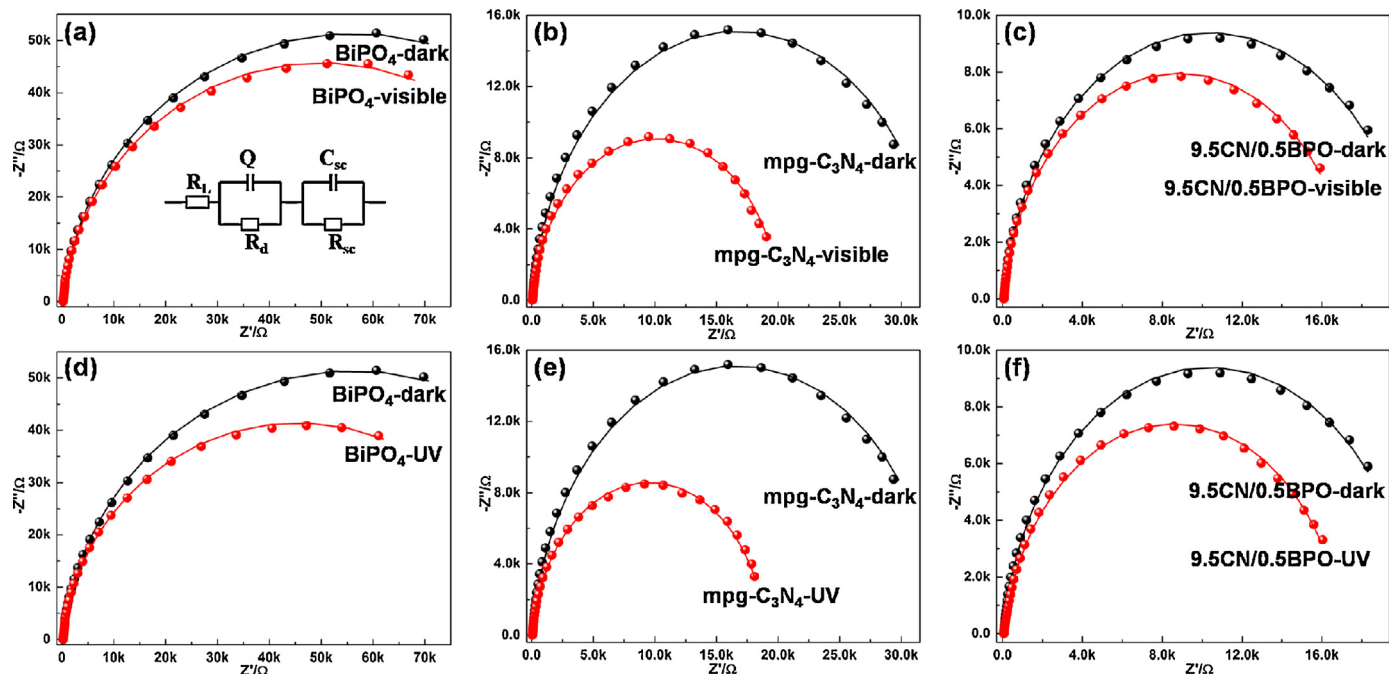
Fig. 14. Nyquist impedance plots of the $BiPO_4$, mpg-C_3N_4 and 9.5CN/0.5BPO electrodes measured in 0.1 M Na_2SO_4. The solid line traces corresponded to the fitting using the equivalent circuit in the inset of Fig. 14a.

Table 3
Fitted parameters of the EIS of $BiPO_4$, mpg-C_3N_4 and 9.5CN/0.5BPO.

CDC code	R_L (Ω)	R_d (Ω)	C (F)	R_{sc} (kΩ)	Q (Ssec^n)	n
$BiPO_4$ (dark)	125.6	101.3	1.358×10^{-8}	111.7	2.152×10^{-5}	0.9466
$BiPO_4$ (visible)	114.4	113.2	1.173×10^{-8}	99.62	2.134×10^{-5}	0.9458
$BiPO_4$ (UV)	138.0	79.15	1.977×10^{-8}	90.54	2.330×10^{-5}	0.9437
mpg-C_3N_4 (dark)	54.16	20.56	1.099×10^{-7}	33.18	2.432×10^{-5}	0.9409
mpg-C_3N_4 (visible)	38.73	35.91	5.030×10^{-8}	20.09	2.414×10^{-5}	0.9355
mpg-C_3N_4 (UV)	54.17	20.67	1.094×10^{-7}	18.94	2.515×10^{-5}	0.9375
9.5CN/0.5BPO (dark)	46.12	27.09	7.286×10^{-8}	20.61	2.437×10^{-5}	0.9412
9.5CN/0.5BPO (visible)	44.08	29.23	6.553×10^{-8}	17.55	2.526×10^{-5}	0.9381
9.5CN/0.5BPO (UV)	48.70	25.06	6.790×10^{-8}	17.02	2.679×10^{-5}	0.9116

adsorbed onto the surface of $BiPO_4$/mpg-C_3N_4 and reduce it to form $\bullet O_2^-$ because the CB edge potentials of $BiPO_4$ (−0.61 eV) and mpg-C_3N_4 (−0.89 eV) were more negative than the potential of $O_2/\bullet O^{2-}$ (−0.33 eV) [87], which was capable for the degradation of RhB. At the same time, the holes left behind in the VB of mpg-C_3N_4 could not directly oxidize OH^- or H_2O to form $\bullet OH$, as the VB edge potential of mpg-C_3N_4 (+1.92 eV) was more negative than the potentials of $\bullet OH/H_2O$ (+2.68 eV) and $\bullet OH/OH^-$ (+1.99 eV) [88]. Subsequently, the reactive species including $\bullet O_2^-$ and h^+ participated in the photocatalytic reaction. The active species trapping experiment results also proved that $\bullet O_2^-$ and h^+ were the primary active species determining visible light catalysis activity.

Under UV light irradiation (Fig. 16b), both mpg-C_3N_4 and $BiPO_4$ could be excited to generate electrons and holes. Then some of the photogenerated electrons in the CB of mpg-C_3N_4 could transfer to the CB of $BiPO_4$ via the well developed $BiPO_4$/mpg-C_3N_4 interface because the CB edge potential of mpg-C_3N_4 (−0.89 eV) was more negative than that of $BiPO_4$ (−0.61 eV). While at the same time, since the VB edge potential of $BiPO_4$ (+3.22 eV) was more positive than that of mpg-C_3N_4 (+1.92 eV), some of the photogenerated holes would transfer from the VB of $BiPO_4$ to that of mpg-C_3N_4 through the well-defined interface between $BiPO_4$ and mpg-C_3N_4. As a result, the recombination of photogenerated hole-electron pairs was inhibited [89]. Therefore, the electrons in the CB of both $BiPO_4$ (−0.61 eV) and mpg-C_3N_4 (−0.89 eV) could react with O_2 to
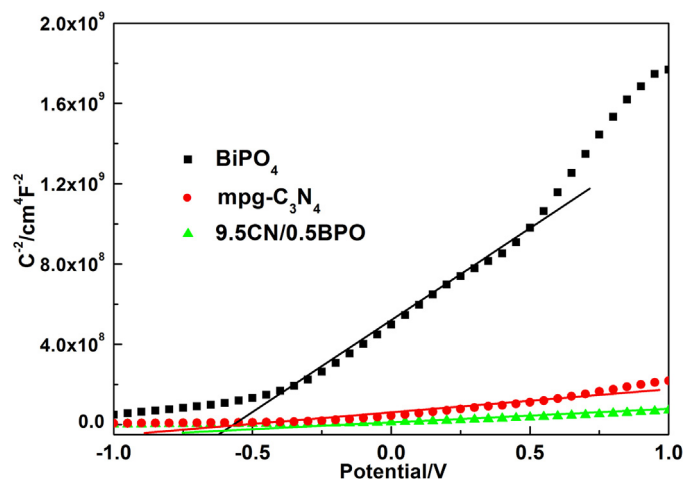

Fig. 15. Mott-Schottky plots of $BiPO_4$, mpg-C_3N_4 and 9.5CN/BPO.

generate $\bullet O_2^-$ because the CB edge potentials of $BiPO_4$ and mpg-C_3N_4 were more negative than the potential of $O_2/\bullet O^{2-}$ (−0.33 eV) [87], which could further react with RhB. Meanwhile, the holes in the VB of both $BiPO_4$ and mpg-C_3N_4 could directly oxidize RhB. Furthermore, the holes in the VB of $BiPO_4$ could react with OH^- or H_2O
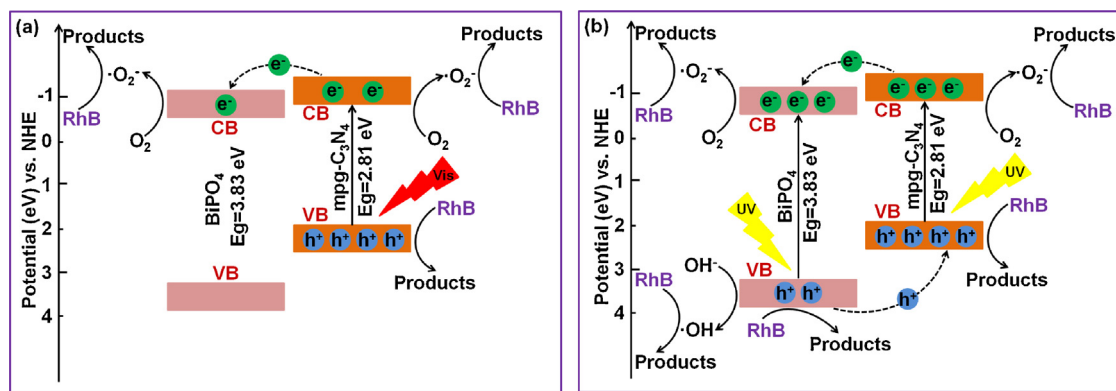
Fig. 16. Schematic diagram of charge transfer and separation and the possible photocatalytic mechanism over mpg-C_3N_4/BiPO$_4$ heterojunctions under (a) visible and (b) UV light irradiation.

to produce $\bullet$OH because the VB edge potential of BiPO$_4$ (+3.22 eV) was more positive than the potentials of $\bullet$OH/H$_2$O (+2.68 eV) and $\bullet$OH/OH$^-$ (+1.99 eV) [88], and then induced the RhB degradation. Therefore, various highly active species including $\bullet$O$_2^-$, h$^+$ and $\bullet$OH simultaneously participated in the photocatalytic reaction. The active species trapping experiment results also proved that $\bullet$O$_2^-$, h$^+$ and $\bullet$OH were the primary active species determining UV light catalysis activity.

4. Conclusions

To summarize, we have successfully prepared highly efficient mpg-C_3N_4/BiPO$_4$ heterostructured photocatalysts by the facile ultrasonic chemical method. The mpg-C_3N_4/BiPO$_4$ composites exhibited enhanced visible, UV and sun light photocatalytic activities toward the degradation of RhB as compared to mpg-C_3N_4 and BiPO$_4$. The optimum photocatalytic activity of 9.5CN/0.5BPO for the degradation of RhB was 1.3 and 1.2 times as high as that of mpg-C_3N_4 under visible and solar light irradiation, respectively, and was 4.2 and 1.5 times higher than those of mpg-C_3N_4 and BiPO$_4$, respectively, under UV light irradiation. However, a mechanically mixed 9.5 M CN/0.5BPO showed lower photocatalytic activity than that of 9.5CN/0.5BPO. The enhanced photocatalytic activity could be attributed to the electrostatic interaction between mpg-C_3N_4 and BiPO$_4$ by forming an intimate mpg-C_3N_4/BiPO$_4$ heterostructure, which could result in the improved photogenerated charge separation efficiency as confirmed by the photocurrent and electrochemical impedance spectra (EIS), and further improvement of photocatalytic activity. Mpg-C_3N_4/BiPO$_4$ composites had no-selectivity and could effectively degrade three organic dyes. Moreover, the active species trapping experiments indicated that $\bullet$O^{2-} and h$^+$ were the main active species under visible light irradiation, whereas $\bullet$O$_2^-$, h$^+$ and $\bullet$OH were the main active species under UV light irradiation. This study may provide a facile way to design efficient heterostructured photocatalysts.

Acknowledgments

Appendix A. Supplementary data

Supplementary data associated with this article can be found, in the online version, at http://dx.doi.org/10.1016/j.apcatb.2017.02.025.

References

[1] Y.F. Chen, W.X. Huang, D.L. He, Y. Situ, H. Huang, ACS Appl. Mater. Interfaces 6 (2014) 14405–14414.
[2] M. Xu, L. Han, S.J. Dong, ACS Appl. Mater. Interfaces 5 (2013) 12533–12540.
[3] F.T. Li, Y.B. Xue, B. Li, Y.J. Hao, X.J. Wang, R.H. Liu, J. Zhao, Ind. Eng. Chem. Res. 53 (2014) 19540–19549.
[4] S.B. Wang, J.L. Lin, X.C. Wang, Phys. Chem. Chem. Phys. 16 (2014) 14656–14660.
[5] S.B. Wang, X.C. Wang, Small 11 (2015) 3097–3112.
[6] S.B. Wang, W.S. Yao, J.L. Lin, Z.X. Ding, X.C. Wang, Angew. Chem. Int. Ed. 53 (2014) 1034–1038.
[7] S.B. Wang, X.C. Wang, Angew. Chem. Int. Ed. 55 (2016) 2308–2320.
[8] S.B. Wang, X.C. Wang, Appl. Catal. B Environ. 162 (2015) 494–500.
[9] C. Chang, L.Y. Zhu, S.F. Wang, X.L. Chu, L.F. Yue, ACS Appl. Mater. Interfaces 6 (2014) 5083–5093.
[10] C.S. Pan, J. Xu, Y.J. Wang, D. Li, Y.F. Zhu, Adv. Funct. Mater. 22 (2012) 1518–1524.
[11] C.S. Pan, Y.F. Zhu, Environ. Sci. Technol. 44 (2010) 5570–5574.
[12] C.S. Pan, Y.F. Zhu, J. Mater. Chem. 21 (2011) 4235–4241.
[13] H.F. Shi, G.Q. Chen, C.L. Zhang, Z.G. Zou, ACS Catal. 4 (2014) 3637–3643.
[14] H. Xu, Y.G. Xu, H.M. Li, J.X. Xia, J. Xiong, S. Yin, C.J. Huang, H.L. Wan, Dalton Trans. 41 (2012) 3387–3394.
[15] F.F. Duo, Y.W. Wang, X.M. Mao, X.C. Zhang, Y.F. Wang, C.M. Fan, Appl. Surf. Sci. 340 (2015) 35–42.
[16] X. Lin, D. Liu, X.Y. Guo, N. Sun, S. Zhao, L.M. Chang, H.J. Zhai, Q.W. Wang, J. Phys. Chem. Solids 76 (2015) 170–177.
[17] H.F. Ye, H.L. Lin, J. Cao, S.F. Chen, Y. Chen, J. Mol. Catal. A Chem. 397 (2015) 85–92.
[18] T. Lv, L.K. Pan, X.J. Liu, Z. Sun, RSC Adv. 2 (2012) 12706–12709.
[19] X.C. Wang, K. Maeda, A. Thomas, K. Takanabe, G. Xin, J.M. Carlsson, K. Domen, M. Antonietti, Nat. Mater. 8 (2009) 76–82.
[20] D.D. Zheng, C.Y. Pang, X.C. Wang, Chem. Commun. 51 (2015) 17467–17470.
[21] D.D. Zheng, G.G. Zhang, Y.D. Hou, X.C. Wang, Appl. Catal. A Gen. 521 (2016) 2–8.
[22] Z.A. Lan, G.G. Zhang, X.C. Wang, Appl. Catal. B Environ. 192 (2016) 116–125.
[23] D.D. Zheng, G.G. Zhang, X.C. Wang, Appl. Catal. B Environ. 179 (2015) 479–488.
[24] X.J. Wang, W.Y. Yang, F.T. Li, Y.B. Xue, R.H. Liu, Y.J. Hao, Ind. Eng. Chem. Res. 52 (2013) 17140–17150.
[25] Y.M. He, J. Cai, L.H. Zhang, X.X. Wang, H.J. Lin, B.T. Teng, L.H. Zhao, W.Z. Weng, H.L. Wan, M.H. Fan, Ind. Eng. Chem. Res. 53 (2014) 5905–5915.
[26] J.N. Qin, S.B. Wang, H. Ren, Y.D. Hou, X.C. Wang, Appl. Catal. B Environ. 179 (2015) 1–8.
[27] Y. Zheng, L.H. Lin, B. Wang, X.C. Wang, Angew. Chem. Int. Ed. 54 (2015) 12868–12884.
[28] J.S. Zhang, Y. Chen, X.C. Wang, Energy Environ. Sci. 8 (2015) 3092–3108.
[29] L.H. Lin, H.H. Ou, Y.F. Zhang, X.C. Wang, ACS Catal. 6 (2016) 3921–3931.
[30] Y. Zheng, J. Liu, J. Liang, M. Jaroniec, S.Z. Qiao, Energy Environ. Sci. 5 (2012) 6717–6731.
[31] A. Habibi-Yangjeh, A. Akhundi, J. Mol. Catal. A Chem. 415 (2016) 122–130.
[32] S.W. Cao, J.G. Yu, J. Phys. Chem. Lett. 5 (2014) 2101–2107.
[33] Z.S. Li, S.Y. Yang, J.M. Zhou, D.H. Li, X.F. Zhou, C.Y. Ge, Y.P. Fang, Chem. Eng. J. 241 (2014) 344–351.

[34] E.Z. Lee, Y.S. Jun, W.H. Hong, A. Thomas, M.M. Jin, Angew. Chem. Int. Ed. 49 (2010) 9706–9710.
[35] Y. Wang, X.C. Wang, M. Antonietti, Y.J. Zhang, ChemSusChem 3 (2010) 435–439.
[36] Y.J. Cui, J.S. Zhang, G.G. Zhang, J.H. Huang, P. Liu, M. Antonietti, X.C. Wang, J. Mater. Chem. 21 (2011) 13032–13039.
[37] J. Xu, Y.J. Wang, Y.F. Zhu, Langmuir 29 (2013) 10566–10572.
[38] G. Liu, P. Niu, C.H. Sun, S.C. Smith, Z.G. Chen, G.Q. Lu, H.M. Cheng, J. Am. Chem. Soc. 132 (2010) 11642–11648.
[39] X.C. Wang, X.F. Chen, A. Thomas, X.Z. Fu, M. Antonietti, Adv. Mater. 21 (2009) 1609–1612.
[40] S.X. Min, G.X. Lu, J. Phys. Chem. C 116 (2012) 19644–19652.
[41] Y.X. Yang, Y.N. Guo, F.Y. Liu, X. Yuan, Y.H. Guo, S.Q. Zhang, W. Guo, M.X. Huo, Appl. Catal. B Environ. 142 (2013) 828–837.
[42] L. Ge, C.C. Han, J. Liu, Appl. Catal. B Environ. 108 (2011) 100–107.
[43] K. Sridharan, E. Jang, T.J. Park, Appl. Catal. B Environ. 142 (2013) 718–728.
[44] J.X. Sun, Y.P. Yuan, L.G. Qiu, X. Jiang, A.J. Xie, Y.H. Shen, J.F. Zhu, Dalton. Trans. 41 (2012) 6756–6763.
[45] X.J. Zou, Y.Y. Dong, X.Y. Li, Q.D. Zhao, Y.B. Cui, G. Lu, Catal. Commun. 69 (2015) 109–113.
[46] Z.S. Li, S.Y. Yang, J.M. Zhou, D.H. Li, X.F. Zhou, C.Y. Ge, Y.P. Fang, Chem. Eng. J. 241 (2014) 344–351.
[47] Z.S. Li, B.L. Li, S.H. Peng, D.H. Li, S.Y. Yang, Y.P. Fang, RSC Adv. 4 (2014) 35144–35148.
[48] F. Goettmann, A. Fischer, M. Antonietti, A. Thomas, Angew. Chem. Int. Ed. 45 (2006) 4467–4471.
[49] L. Ge, F. Zuo, J.K. Liu, Q. Ma, C. Wang, D.Z. Sun, L. Bartels, P.Y. Feng, J. Phys. Chem. C 116 (2012) 13708–13714.
[50] Y.M. He, J. Cai, T.T. Li, Y. Wu, Y.M. Yi, M.F. Luo, L.H. Zhao, Ind. Eng. Chem. Res. 51 (2012) 14729–14737.
[51] S. Chauhan, M. Kumar, S. Chhoker, S.C. Katyal, H. Singh, M. Jewariya, K.L. Yadav, Solid State Commun. 152 (2012) 525–529.
[52] W.J. Shan, Y. Hu, Z.G. Bai, M.M. Zheng, C.H. Wei, Appl. Catal. B Environ. 188 (2016) 1–12.
[53] X.F. Li, J. Zhang, L.H. Shen, Y.M. Ma, W.W. Lei, Q.L. Cui, G.T. Zou, Appl. Phys. A Mater. 94 (2009) 387–392.
[54] Y.A. Li, J. Zhang, Q.S. Wang, Y.X. Jin, D.H. Huang, Q.L. Cui, G.T. Zou, J. Phys. Chem. B 114 (2010) 9429–9434.
[55] Y.P. Zhu, M. Li, Y.L. Liu, T.Z. Ren, Z.Y. Yuan, J. Phys. Chem. C 118 (2014) 10963–10971.
[56] M.L. Zhao, G.S. Li, L.P. Li, L.S. Yang, J. Zheng, Cryst. Growth Des. 12 (2012) 3983–3991.
[57] M. Saadoun, B. Bessaïs, N. Mliki, M. Ferid, H. Ezzaouia, R. Bennaceur, Appl. Surf. Sci. 210 (2003) 240–248.
[58] H.P. Li, J.Y. Liu, W.G. Hou, N. Du, R.J. Zhang, X.T. Tao, Appl. Catal. B Environ. 160 (2014) 89–97.
[59] H.F. Ye, H.L. Lin, J. Cao, S.F. Chen, Y. Chen, J. Mol. Catal. A Chem. 397 (2015) 85–92.
[60] X. Song, Y. Hu, M.M. Zheng, C.H. Wei, Appl. Catal. B Environ. 182 (2016) 587–597.
[61] X.J. Bai, L. Wang, R.L. Zong, Y.F. Zhu, J. Phys. Chem. C 117 (2013) 9952–9961.
[62] H. Katsumata, T. Sakai, T. Suzuki, S. Kaneco, Ind. Eng. Chem. Res. 53 (2014) 8018–8025.
[63] Z.Y. Zhang, D.L. Jiang, D. Li, M.Q. He, M. Chen, Appl. Catal. B Environ. 183 (2016) 113–123.
[64] Y. Huang, Z.H. Ai, W.K. Ho, M.J. Chen, S.C. Lee, J. Phys. Chem. C 114 (2010) 6342–6349.
[65] C. Chang, Y. Fu, M. Hu, C.Y. Wang, G.Q. Shan, L.Y. Zhu, Appl. Catal. B Environ. 142 (2013) 553–560.
[66] J. Xu, G.X. Wang, J.J. Fan, B.S. Liu, S.W. Cao, J.G. Yu, J. Power Sources 274 (2015) 77–84.
[67] C.S. Pan, D. Li, X.G. Ma, Y. Chen, Y.F. Zhu, Catal. Sci. Technol. 1 (2011) 1399–1405.
[68] D.M. Chen, K.W. Wang, W.Z. Hong, R.L. Zong, W.Q. Yao, Y.F. Zhu, Appl. Catal. B Environ. 166 (2015) 366–373.
[69] Y.M. He, Y. Wang, L.H. Zhang, B.T. Teng, M.H. Fan, Appl. Catal. B Environ. 168 (2015) 1–8.
[70] Y. Mi, L.Y. Wen, Z.J. Wang, D.W. Cao, Y.G. Fang, Y. Lei, Appl. Catal. B Environ. 176 (2015) 331–337.
[71] X.S. Zhang, K. Tian, J.Y. Hu, H. Jiang, Chemosphere 141 (2015) 127–133.
[72] H.B. Fu, S.C. Zhang, T.G. Xu, Y.F. Zhu, J.M. Chen, Environ. Sci. Technol. 42 (2008) 2085–2091.
[73] Y.C. Deng, L. Tang, G.M. Zeng, J.J. Wang, Y.Y. Zhou, J.J. Wang, J. Tang, Y.N. Liu, B. Peng, F. Chen, J. Mol. Catal. A Chem. 421 (2016) 209–221.
[74] P.X. Lei, C.C. Chen, J. Yang, W.H. Ma, J.C. Zhao, Z. Ling, Environ. Sci. Technol. 39 (2005) 8466–8474.
[75] K. Yu, S.G. Yang, H. He, C. Sun, C.G. Gu, Y.M. Ju, J. Phys. Chem. A 113 (2009) 10024–10032.
[76] C.S. Zhu, L. Zhang, B. Jiang, J.T. Zheng, P. Hu, S.J. Li, M.B. Wu, W.T. Wu, Appl. Surf. Sci. 377 (2016) 99–108.
[77] Y.Y. Zhu, Y.J. Wang, Q. Ling, Y.F. Zhu, Appl. Catal. B Environ. 200 (2017) 222–229.
[78] H. Ji, F. Chang, X. Hu, W. Qin, J. Shen, Chem. Eng. J. 218 (2013) 183–190.
[79] W.Y. Lu, T.F. Xu, Y. Wang, H.G. Hu, N. Li, X.M. Jiang, W.X. Chen, Appl. Catal. B Environ. 180 (2016) 20–28.
[80] Y.J. Lin, S. Zhou, X.H. Liu, S. Sheehan, D.W. Wang, J. Am. Chem. Soc. 131 (2009) 2772–2773.
[81] H.B. Fu, T.G. Xu, S.B. Zhu, Y.F. Zhu, Environ. Sci. Technol. 42 (2008) 8064–8069.
[82] H.T. Yu, X. Quan, S. Chen, H.M. Zhao, Y.B. Zhang, J. Photochem. Photobiol. A 200 (2008) 301–306.
[83] F.X. Xiao, S.F. Hung, H.B. Tao, J.W. Miao, H.B. Yang, B. Liu, Nanoscale 6 (2014) 14950–14961.
[84] S.L. Ma, S.H. Zhan, Y.N. Jia, Q. Shi, Q.X. Zhou, Appl. Catal. B Environ. 186 (2016) 77–87.
[85] M. Zhang, X.J. Bai, D. Liu, J. Wang, Y.F. Zhu, Appl. Catal. B Environ. 164 (2015) 77–81.
[86] H. Maeda, K. Ikeda, K. Hashimoto, K. Ajito, M. Morita, A. Fujishima, J. Phys. Chem. B 103 (1999) 3213–3217.
[87] M. Ou, Q. Zhong, S.L. Zhang, L.M. Yu, J. Alloy Compd. 626 (2015) 401–409.
[88] Y.M. He, L.H. Zhang, B.T. Teng, M.H. Fan, Environ. Sci. Technol. 49 (2015) 649–656.
[89] G.Y. Li, X. Nie, J.Y. Chen, Q. Jiang, T.C. An, P.K. Wong, H.M. Zhang, H.J. Zhao, H. Yamashita, Water Res. 86 (2015) 17–24.